1 2 9 0

UNIVERSIDADE Ð
COIMBRA

Matilde de Matos Simões

X-ray Imaging with a Single-pixel detector

September 2023

X-ray Imaging with a Single-Pixel Detector

Matilde de Matos Simões

Thesis submitted to the Faculty of Sciences and Technology of the University of Coimbra
for the degree of Master in Physics Engineering

Supervisors:

Doutor Pedro Guilherme da Cunha Leitão Dias Vaz (Laboratory for Instrumentation, Biomedical
Engineering and Radiation Physics, University of Coimbra)

Doutor Pedro Hugo Ferreira Natal da Luz (Institute of Experimental and Applied Physics of the
Czech Technical University in Prague)

Doutor André Filipe Ventura Cortez (Nicolaus Copernicus Astronomical Center of the
Polish Academy of Sciences)

Department of Physics
Faculty of Sciences and Technology of the University of Coimbra

Coimbra, September 2023

This work was developed in collaboration with:

Abstract

X-ray imaging is an invaluable tool for noninvasive analysis in many fields ranging from basic science to medicine and security. The development of low-dose large area imaging solutions still represents an important challenge for various applications. One solution to the imaging of large areas lies in the development of novel computational imaging systems that can overcome the limitations imposed by hardware, relying instead on numerical processing power. The single-pixel detector, depending on the application, may offer a competitive edge over conventional cameras (being a cheaper alternative to the multi-pixelated solutions). In addition, the single-pixel detector can be used to achieve improved geometry detection acceptance, faster timing response, and good spatial resolution with low radiation dose. These features make single-pixel detectors an interesting solution for applications where the detected intensities are very weak due to scattering or absorption losses, for example medical imaging or long-range 3D imaging. Finally, the single-pixel detectors combined with compressive sensing can significantly reduce the data storage and data transfer requirements, an important consideration for remote sensing applications or when the problem is high dimensional such as hyperspectral imaging.

A single-pixel camera is a technology that produces images by interrogating a scene with a series of spatially resolved patterns while measuring the correlated intensity on a detector without spatial resolution. Fundamentally, it performs a type of polymorphic scanning to sense intensity information from many places at once. The potential of this approach is the ability to recover a multi-pixel image faster than the traditional scan-based methods, and further benefits from the commercially available technology.

In this work, we explore the application of *Single-Pixel Imaging* (*SPI*) techniques to produce two-dimensional images, using a detector with one pixel only. On a first stage, simulation tools were used to define the appropriate material and thickness for the masks, by calculating the transmission of different cases. Regarding this step and the cost and amount of material to use, $5\,\text{mm}$ *Polylactic Acid Filament* (*PLA*) masks were printed. On a second stage, the entire system was simulated with sources with different energy distributions and different mask thicknesses. Afterwards, an experimental system with a triple cascade of *Gas Electron Multiplier* (*GEM*) plates with an active area of $10 \times 10 \text{ cm}^2$ was assembled. The setup, based on the application of Hadamard patterns, showed promising results, proving the ability of the system to acquire 4×4 pixel images using *PLA* masking.

Both simulation, using *GEANT4*, and experimental setup, used in this work to demonstrate this technique will be reported here along with the first results combining X-ray *SPI* , with fast-prototyping masks and a gaseous detector.

Resumo

A imagiologia de raios-X é uma ferramenta inestimável para análises não invasivas em diversas áreas de investigação, desde a ciência básica até à medicina e segurança. O desenvolvimento de soluções de imagiologia para grandes áreas com doses reduzidas de radiação ainda representa um desafio importante em várias aplicações. Uma solução para tal foca-se na criação de novos sistemas de imagiologia computacional que possam superar as limitações impostas pelo hardware, dependendo em vez disso do poder de processamento computacional. Um detector de pixel único, dependendo da aplicação, pode oferecer uma vantagem competitiva sobre as câmaras convencionais (sendo uma alternativa mais barata às soluções multipixeladas). Além disso, o detector de pixel único pode ser usado para alcançar uma melhor aceitação geométrica de deteção, um tempo de aquisição mais curto e boa resolução espacial com uma dose reduzida de radiação. Essas características tornam os detectores de pixel único uma solução intrigante para aplicações em que as intensidades detectadas são muito fracas devido a perdas por dispersão ou absorção, como em imagens médicas ou imagens 3D de longo alcance. Por fim, os detectores de pixel único juntamente com *Compressive Sensing* (*CS*) podem reduzir significativamente os requisitos de armazenamento e transferência de dados, uma consideração importante para aplicações de deteção remota ou, nos casos em que o problema é de multi-dimensionalidade, como em imagiologia hiperespectral.

Uma câmara de pixel único é uma tecnologia que produz imagens ao irradiar uma cena com uma série de padrões, enquanto determina a intensidade correlacionada com um detector sem resolução espacial. Essencialmente, esta câmara realiza um tipo de scanning polimórfico para captar informações da intensidade de vários pontos simultaneamente. O potencial deste método está na capacidade de recuperar uma imagem multipixel com um tempo de aquisição menor do que os métodos tradicionais baseados em scanning e ainda beneficia da tecnologia comercialmente disponível.

Neste trabalho, exploramos a aplicação da técnica de imagiologia com um detetor de pixel único para produzir imagens bidimensionais, usando um detector com apenas um píxel. Numa primeira fase, foram utilizadas ferramentas de simulação para definir o material adequado e a espessura das máscaras, calculando a transmissão para diferentes casos. Tendo em consideração esta etapa e o custo/quantidade de material a ser usado, máscaras de *PLA* com 5 mm foram impressas numa impressora 3D. Numa segunda fase, todo o sistema foi simulado com fontes com diferentes distribuições de energia e diferentes espessuras de máscara. Posteriormente, um sistema experimental com um detetor

constituído por uma área ativa de 10×10 cm^2 e uma região de amplificação com recurso a 3 *GEM*s foi desenvolvido. O setup, baseado na aplicação de padrões de Hadamard, apresentou resultados promissores, comprovando a capacidade do sistema de adquirir imagens de 4×4 píxeis usando máscaras de *PLA*.

Tanto as simulações, utilizando o *GEANT4*, quanto o setup experimental, utilizados neste trabalho para demonstrar esta técnica, serão relatados aqui, bem como os primeiros resultados aplicando imagiologia de detetores de píxel único a raios-X, desenvolvido recorrendo a técnicas de prototipagem rápida e um detector gasoso.

Acknowledgements

Em primeiro lugar, quero agradecer aos meus orientadores. Ao Dr. Pedro Vaz e ao Dr. André Cortez que me acompanharam desde o início e proporcionaram uma oportunidade de trabalhar num projeto internacional e diferente do que esperaria para a minha tese. Ao Dr. Hugo Natal da Luz, que se juntou depois e não tinha obrigação de me ajudar, e tanto me ajudou. Obrigada pela dedicação e paciência aos três.

Aos meus amigos de secundário, JECDP, muitos que já me acompanham desde o 5º ano, foi um privilégio crescer convosco. Mesmo com percursos diferentes, foram sempre um pilar neste percurso, não tenho a mínima dúvida que após esta etapa continuarão sempre a ser um grande apoio e companhia. Agradeço também às minhas amigas da canoagem, evoluímos juntas e ensinaram me a ter motivação mesmo quando nenhuma de nós via um fim.

Aos meus amigos da universidade, principalmente aos Cruzados, fizeram me ver Coimbra de maneira diferente e melhor. Com vocês, fiz as memórias dos melhores momentos e tive apoio constante nos piores momentos. Obrigada por Cruzarem a minha vida. Agradeço também aos meus padrinhos e madrinhas, afilhadas e afilhado, netas e netos, (...), são todos muito importantes para mim. À Íris e à Maria, deixo um abraço especial.

Um grande obrigada ao David, por todo o carinho e paciência para me aturar.

Por fim, quero agradecer muito à minha família. Aos meus pais, que me ajudam mesmo quando decido ir estudar a 2000km de casa. Ao Gui, que me mostra cada vez mais que não vai ser um curso universitário que me vai limitar e ao Dani, que vai ficar a cuidar do DF por mim.

A estes todos, e muitos mais só posso agradecer.

Contents

List of Figures

List of Tables

Acronyms

Chapter 1

Introduction

1.1 Context and Motivation

X-rays were discovered by Röntgen [1], in the end of the 19$^{\text{th}}$ century. Its nature, makes of X-rays an invaluable tool for noninvasive analysis in many fields ranging from basic science to medicine, engineering and security [2, 3], because of its ability to penetrate through matter.

In the last century, many advancements have been made in the field of X-ray imaging. Although, there are still some limitations to be considered, in particular in applications related to medical imaging. X-ray radiation poses a risk to human health by harming human body tissues, so it is crucial to achieve low-dose imaging, avoiding overexposure. The same applies to other biological tissues and materials [3]. Another important issue is related to the scattering that occurs after the X-rays pass through the sample, which can be detrimental to image quality by introducing noise [4]. Although, large area high resolution X-ray imaging has already been achieved, the cost and complexity to develop safe X-ray imaging systems is very high.

An alternative, cost-efficient, with improved detection efficiency, faster timing response, and good spatial resolution with low radiation dose is presented in this work. The techniques explored for X-ray imaging in this work is based on the so-called *Single-Pixel Imaging (SPI)*. This technique relies on numerical processing power to achieve higher resolution images, instead of complex hardware. By using a single-pixel detector and a light/radiation modulator to project a set of patterns, *SPI* presents itself as a cost-effective option to multi-pixelated ones [5]. In addition, the single-pixel detector can be used to achieve improved geometry detector acceptance, given the large one pixel area of detection, and removing the non-active areas between pixels. In certain conditions, it can also obtain faster timing response [6] when compared with frame-based

readout [7]. Moreover, this technique enables detectors to image through diffuse media, since the detector integrates all the transmitted radiation for each mask. Each mask measurement suffers an equal attenuation, resulting in the preservation of the intensity relation between the masks [8].

By combining this technique with *Compressive Sensing* (*CS*), it is possible to further reduce the data storage and data transfer requirements, since *CS* states that an image can be reconstructed with a smaller number of measurements than the amount of pixels, under certain conditions [9]. This reduction in the number of measurements can allow for a reduction in radiation dose [7]. This can be useful for remote sensing applications and all applications of hyperspectral imaging.

1.2 Objectives

The main objective of this work is to further study the feasibility of *SPI* with X-ray radiation. For that, a *SPI* prototype was simulated in *GEANT4* and built experimentally. In order to perform this work, a detector was developed. This detector based on a standard triple-*Gas Electron Multiplier* (*GEM*) configuration, has an active area of 10×10 cm^2 and was operated with a mixture of Ar/CO_2 70/30 at atmospheric pressure. Its performance assessment including the characterization in terms of gain, energy resolution and uniformity in area and in time, also was part of the objectives of this work. The set of patterns applied were based in the Hadamard matrix and 3D printed in 5 mm *Polylactic Acid Filament* (*PLA*) masks, testing a new material and manufacturing process for the light modulator. Measurements were performed for different acquisition times per mask, in order to obtain 4×4 pixel images.

This project was organized in two stages:

- **Simulation**: initially, in the first semester, different materials and thicknesses for the masks were studied through simulations. In a more advanced state, the entire *SPI* system was simulated for different energy sources.

- **Experimental work**: during the second semester, all the experimental work was performed at the Van de Graaff laboratory, of the Institute of Experimental and Applied Physics of the Czech Technical University in Prague, Czechia.

1.3 Investigation Team

This project is a collaboration between the Laboratory for Instrumentation, Biomedical Engineering and Radiation Physics (LIBPhys), a research center within the Department of Physics of the University of Coimbra and the Institute of Experimental and Applied Physics of the Czech Technical University in Prague, supervised by Dr. Pedro Guilherme Vaz, on behalf of LIBPhys, Dr. André Filipe Ventura Cortez, on behalf of IEAP CTU in Prague (currently in CAMK PAN Polish Academy of Sciences) and Dr. Hugo Natal da Luz, on behalf of IEAP CTU in Prague. The reason for this collaboration comes from the combination of the knowledge on development of radiation detectors by the IEAP CTU in Prague's group and the knowledge on *SPI* by the LIBPhys UC.

Chapter 2

X-ray Detection

2.1 Interaction of Radiation with Matter

For better understanding of the operation principle of gaseous detectors, it is important to first address how radiation interacts with the material of the detector to be used. The type of interaction will depend on the kind of particle to detect and the gas mixture used. Since, in this work, X-rays are the radiation of interest, its characteristics will be discussed next. Only the interactions relevant for this work will be addressed.

2.1.1 X-rays

Originally discovered by Röntgen, in 1885, X-rays are photons originated from atomic transitions [1]. Their energy, E, is related to its wave frequency, v, by the following equation:

$$E = \hbar v \tag{2.1}$$

where h is the Planck's constant.

There are two processes of X-ray generation: *bremsstrahlung* and characteristic radiation.

Characteristic radiation

If the atom suffers some ionization process and is left in an excited state, with a vacancy in one of its shells, it will rearrange itself in order to return to the fundamental state. So, as an electron moves to fill the gap, there is a release of a characteristic X-ray with energy equal to the difference between the initial and final states of the atom. Therefore, as demonstrated in Figure 2.1, these characteristic radiations have well defined energies, that depend on the type of transition occurred and appear as defined peaks in the spectrum [10, 11].
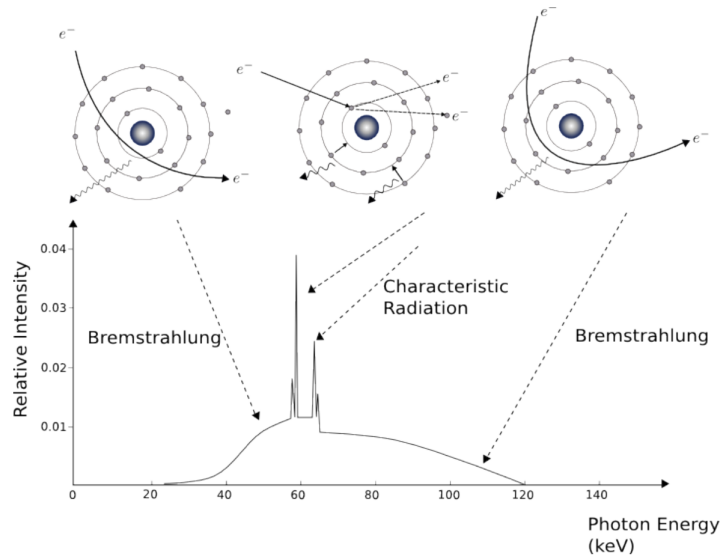
FIGURE 2.1: *Bremsstrahlung* and characteristic radiation mechanisms and their effects on a X-ray spectrum of a tube with a tungsten target. From [11].

Some radioactive isotopes generate X-rays as a byproduct of their radioactive decay. In these scenarios, a type of radioactive decay called electron capture occurs. An inner-shell electron is absorbed by the nucleus, leaving a vacancy in the electronic shell, originating a neutron and a neutrino in the nucleus. When the atomic shells are rearranged as the atom returns to its fundamental state, characteristic radiation is released.

Bremsstrahlung radiation

When a high-energy electron approaches an atomic nucleus, it is decelerated/deflected, losing kinetic energy, emitted as a photon. The farther from the nucleus the interaction occurs, the smaller is the change in electron kinetic energy and the lower is the energy of the photons emitted.

When electrons interact with a certain medium, both processes can occur, and the emission spectrum appears as a continuum of bremsstrahlung radiation superimposed on peaks corresponding to the characteristic energies of the elements. The result is presented in Figure 2.1 [10, 11].

X-ray tubes are devices that generate X-rays by these processes. They consist of a vacuum sealed container with a anode and a cathode inside, as presented in 2.2.
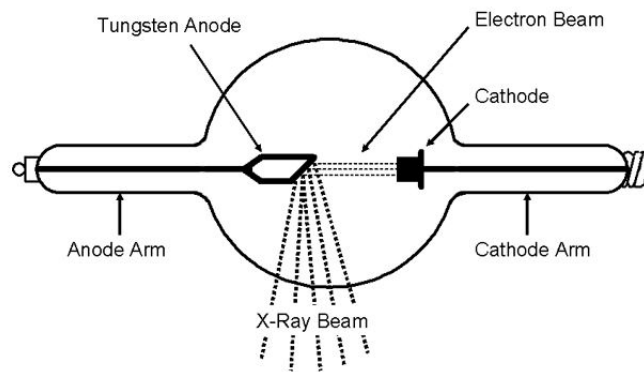
FIGURE 2.2: Schematics of an X-ray tube. From [12].

First, the cathode is heated up, emitting electrons. These are accelerated in the direction of the anode, by applying a high voltage between the cathode and the anode. Finally, as the high energy electrons interact with the anode, either by decelerating and releasing energy in the form of X-ray photons or by ionizing its atoms that emit characteristic X-rays upon returning to their fundamental state [13].

2.1.2 X-ray Interaction with Matter

The operation of X-ray radiation detectors is based on the interaction of the radiation with the detecting medium. This interaction can be through elastic or inelastic processes. The interaction of radiation with matter relevant for this work is essentially made through: photoelectric absorption, predominant for the low-energies used in this work, along with Compton scattering and pair production for higher energies. Depending on the energy of the photon and the material of the target medium (of its atomic number, Z), each interaction has a different relative dominance [10]. Figure 2.3 shows the relevance of the three interactions for different energy ranges and atomic number of the medium as a function of the initial energy of the incident photons.

For low energy photons and for high atomic number materials, the **photoelectric effect** is the predominant mode of interaction. This process consists on a photon being
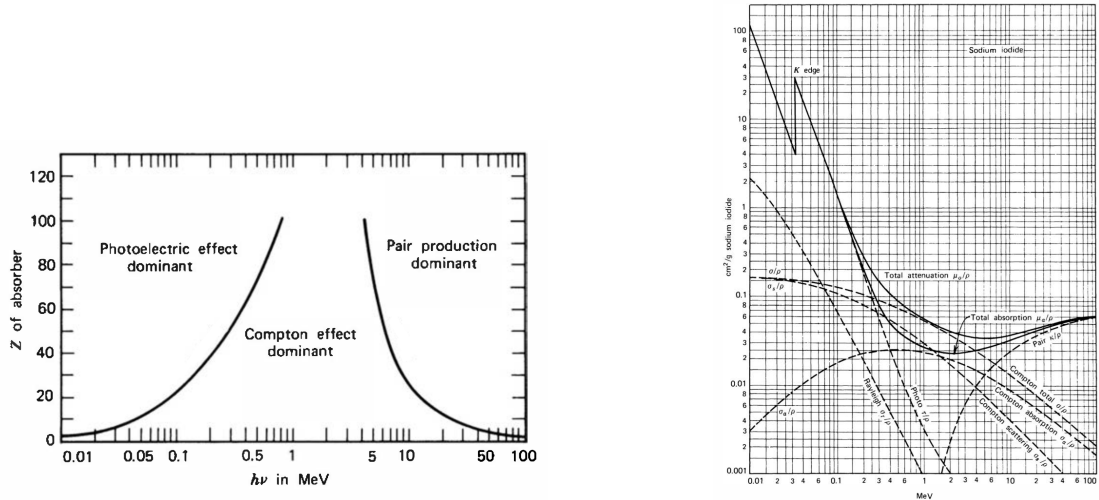
FIGURE 2.3: Left: The relative dominance of the three referred types of X-ray interaction. The lines show the values of Z and E for which the two neighbouring effects are equally probable. From [10]. Right: Cross section for the different X- and gamma-ray interaction processes in sodium iodide as a function of the photon energy. From [10].

absorbed by an atom of a medium and having a photoelectron leaving its bound shell within the atom. The photoelectron is emitted with an energy corresponding to the difference of the incident photon energy and the binding energy, so its energy can be written as:

$$E_e = h\upsilon - E_b \tag{2.2}$$

where the first term of the subtraction is the incident photon energy and E_b is the binding energy of the photoelectron in its original shell. The vacancy left by the emitted photoelectron, leads to the reorganization of the electrons, with an electron filling the vacancy. This transition can result in the emission of characteristic X-rays or in the release of an Auger electron. Figure 2.4 represents the two processes [10].

As the photon energy increases, **Compton scattering** starts to dominate. In this type of interaction, a photon is scattered through a certain angle with respect to the original direction, as indicated in Figure 2.5, carrying only part of its initial energy and transferring the remaining to the recoil electron (assumed to be at rest) that carries the kinetic energy and linear momentum lost by the incident photon [10]. Because all angles
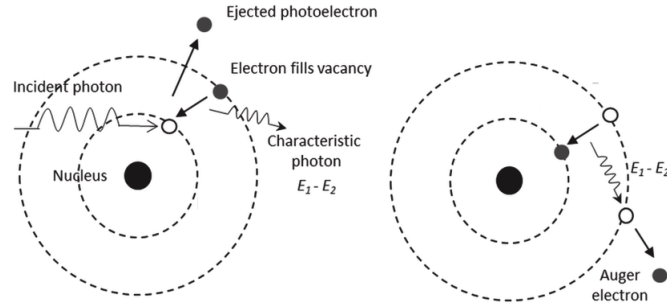
FIGURE 2.4: Schematic representation of the photoelectric effect and formation of characteristic radiation and Auger electron. From [14].

of scattering are possible, the energy transferred to the electron can vary from zero to a large fraction of the initial photon energy. The probability of Compton scattering per atom of the absorber depends on the number of electrons available as scattering targets and is therefore a function of Z. The angular distribution of scattered photons is predicted by the Klein Nishina formula for the differential scattering cross-section $(d\sigma/d\Omega)$ per free electron [10].
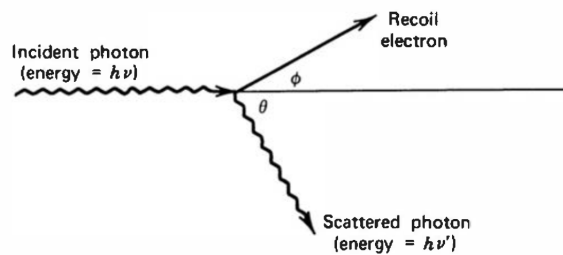
FIGURE 2.5: Schematics of Compton scattering. From [10].

Finally, **pair production** starts to be possible for gamma ray energies larger than the rest-mass energy of an electron-positron pair (1.022 MeV). In this type of interaction, the transformation of a photon into an electron-positron pair occurs, where these two share the excess incident photon energy. The production of secondary byproducts is possible when the positron annihilates in the absorbing medium, and produces normally two annihilation photons. There is no simple expression for the probability of pair production but its magnitude varies approximately with Z^2. This process occurs typically for high-energy gamma-rays. Figure 2.6 illustrates the process described [10]. [1]

---

[1]A process of radiation interaction with a medium not usually discussed is **coherent scattering**. Since low photon energies of below 100 keV will be used, it is also important to discuss this interaction.
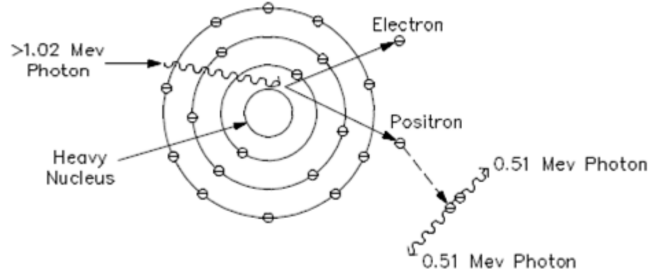
FIGURE 2.6: Schematics of pair production. From [15].

As shown, different processes can occur to a photon while going through the medium, that depend on the media material and the photon energy, that will lead to the attenuation of the photon intensity. The probability of the photon interaction is proportional to the sum of the cross sections of the different possible interactions:

$$\sigma_{total} = \sigma_{photoelectric} + \sigma_{Compton} + \sigma_{pair} \tag{2.3}$$

where, σ_{total} is the total cross section and $\sigma_{photoelectric}$, $\sigma_{Compton}$ and σ_{pair} are the cross sections for the photoelectric effect, Compton scattering and pair production, respectively. By multiplying σ_{total} with the number of atoms per unit volume, an *attenuation coefficient*, μ, is defined. This can be obtained experimentally with equation 2.4, the called Beer-Lambert's law of attenuation.

$$I = I_o e^{-\mu L} \tag{2.4}$$

where I is the intensity of the radiation transmitted, I_o is the intensity of the incident radiation and L is the thickness of a certain absorber. In order to more easily compare the behaviour of different materials, the *mass attenuation coefficient, μ/ρ* ($g\,cm^{-2}$) is more commonly used in literature, since it is independent of the density of the absorber's material.

In this process, the energy transfer to the target material is small and the atoms are not ionized nor excited. The photon interacts coherently with all the electrons of a target atom, changing its direction. As the energy increases, the amount of change in direction decreases. This effect is responsible for scattering, which can influence the resolution of images because X-rays change their trajectory. It can also have some influence on the materials that will be used (such as *Polylactic Acid Filament* (*PLA*)), which, despite absorbing few X-rays, also can cause some scattering.

2.2 Gaseous Detectors

Gaseous radiation detectors display several advantages, being widely used in physics experiments [16]. These detectors take advantage of the interactions of the incident radiation with the chosen filling gas, which originate free electrons and positive ions. A gaseous detector consists on a chamber filled with a pure gas or a gas mixture, containing two or more electrodes.

2.2.1 Operation principle

The primary charge formation in a gaseous detector occurs when a particle or a photon with sufficient energy interacts with the gas molecules within the detector and leading to ionization or excitation. In the case of X-rays, it occurs through the processes already described. These processes originate free electrons and positive ions, that will further ionize and excite atoms of the medium, leading to the formation of the primary charge cloud. This cloud has a number of electrons proportional to the energy deposited by the particle. By dividing the energy of the particle by this number of electrons, we obtain, by definition, the mean energy required to generate an electron-ion pair, commonly referred as the w-value. The number of ion pairs produced for a given energy, exhibits intrinsic fluctuations due to the nature of the interactions involved. As the physical processes involved in primary electron generation are correlated, the variance σ^2, associated with $\overline{n}$, is smaller than what pure Poisson statistics would predict (where $\sigma^2 = \overline{n}$). This difference is characterized by the Fano factor, F. Both these parameters can help understanding the intrinsic energy resolution associated with the energy dissipating mechanisms within detectors. Equations 2.5 and 2.6 indicate how these are calculated.

$$w = \frac{E_{ir}}{\overline{n}} \tag{2.5}$$

$$F = \frac{\text{observed variance in } \overline{n}}{\text{Poisson predicted variance}} \tag{2.6}$$

where E_{ir} is the energy of the incident radiation and $\overline{n}$ is the mean number of electron-ion pairs produced by an ionization radiation when absorbed in the gas [10].

Once the energy has been deposited and transformed into electrons in the detection medium, if a voltage is applied to the electrodes, an electric field is created between

the electrodes, that causes the charges to drift - the electrons towards the anode and the positive ions to the cathode. The movement of these charged particles will induce a current at the electrodes, that can be measured through electronics [10, 17]. During the drift, the electron and ions can suffer recombination, not efficiently separating due to low electric field, and can also attach to gas molecules, forming negative ions. These processes can affect the signal and performance of detectors.

The charge collected varies according to the voltage applied in the electrodes. So for different voltages, the detector assumes a different operation region, as presented in Figure 2.7 [17].
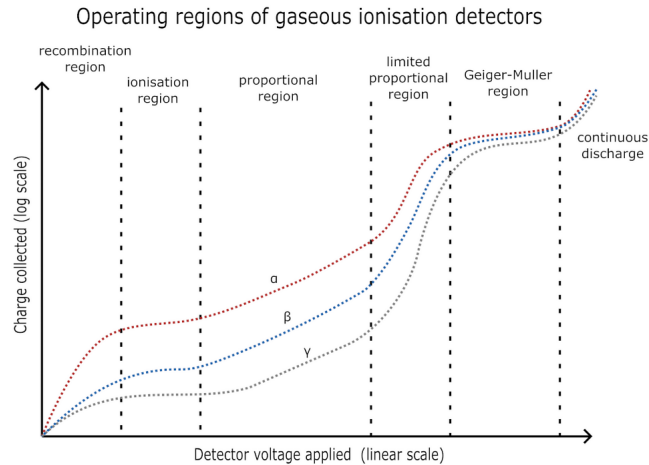
FIGURE 2.7: Operation regions for gaseous detectors for different particles. Red: alpha particles. Blue: beta particles. Grey: gamma particles. From [18].

As can be seen in Figure 2.7, six regions can be distinguished [17]:

1. Recombination region: due to the low applied voltage, the electric field is not strong enough to efficiently separate and accelerate the positive ions from the electrons, so the electron-ion pairs are more susceptible to recombine. As the voltage increases, the recombination rate decreases, eventually becoming zero. No detector operates in this region, since recombination highly affects the signal.

2. Saturation region: in this region, recombination is already negligible and the voltage is still not high enough to produce gas amplification, which leads nearly the totality of the ion pairs produced, to be collect at the electrodes. The ionization

chambers operate in this region. This is also the regime at which the drift (or absorption) regions of the gaseous detectors operate.

3. Proportional region: as the name suggests, in this region, the signal increases proportionally to the applied voltage. This is due to the gas amplification occurring. In this case, the primary electrons gain enough energy from the electric field to originate new ionizations, creating an electron avalanche. So, the number of detected electrons is larger than the number of primary pairs produced, by an amplification factor, dependent of the applied voltage. As this factor remains constant for a given applied voltage and because of the proportionality already mentioned, it allows for different energies of radiation to be distinguished.

4. Limited proportionality region: with the increasing of the voltage, a non linearity in charge mobility occurs, leading to high concentration of positive ions and distortions of the electric field. The proportionality is distorted, so this region is not commonly used in radiation measurement.

5. Geiger-Müller region: in this case, a single interaction can originate multiple avalanches, as the electrons from the primary avalanche gain enough power to produce secondary avalanches. It produces a strong signal similar for all type of incident particles. Geiger-Müller counters are therefore used for particle counting, but not for particle identification.

6. Continuous discharge region: The high voltage applied makes the electric field capable of by itself ionize the gas and produce continuous avalanches, causing continuous discharges.

2.2.2 Detector Development Roadmap

Historically, one of the main breakthroughs in terms of detector development occurred with the introduction of the **Geiger-Müller counters** in the 1920s [19]. These detectors displayed several interesting characteristics such as high sensitivity, wide dynamic range, and easy scalability. Their working principle relied on the Townsend avalanche formation, which takes place when an electron is subject to an intense electric field that allows it to gain enough energy to produce secondary ionization. If the electrons originated by those secondary ionizations also acquire enough kinetic energy, the process will repeat. Only when all free electrons are collected in the anode, the avalanche process stops. This process is schematically presented in Figure 2.8. This type of detector does not allow for energy discrimination, nor particle identification, given that it operates in

a non-proportionality region, as shown in Figure 2.7. Those were later achieved with the **Proportional Ionization Counter**.
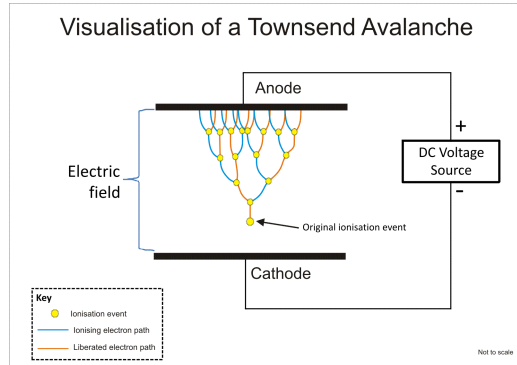
FIGURE 2.8: Townsend avalanche effect between two electrodes. From [20].
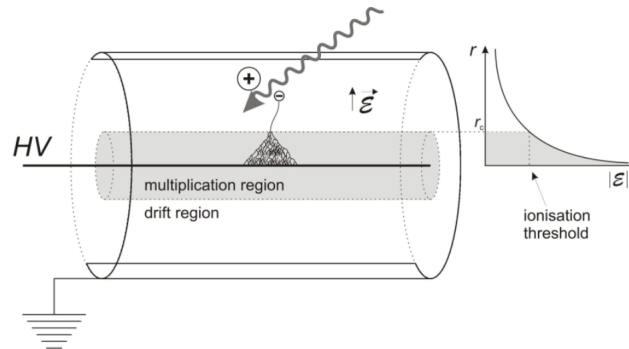
FIGURE 2.9: Schematic of the Gas Proportional Counter. From [21].

*Proportional Ionization Counter*s, introduced in the 1940s, are similar to Geiger-Müller Counters but operate in the proportional region, with significantly lower applied electric field. Its basic geometry is presented in Figure 2.9, with its interior commonly filled with a noble gas. This geometry allows for the definition of a drift region and a multiplication region, due to the radial dependence of the electric field [22]. The multiplication region is confined to a small volume close to the anode, where the electric field is high enough to originate electron avalanches. The rest of the volume (drift region), registers a relatively low electric field, where no multiplication occurs. As a result, electron-ion pairs suffer mostly the same interactions: they are produced in the drift region, as they reach the multiplication region, a single avalanche is formed, producing a signal proportional to the incident radiation [10]. With the additional amplification

stage, in comparison with Ionization Chambers, a wider range of energies can be analysed.

What the researchers found out was that they could improve the signal amplitude and consequently the energy resolution attainable. Still, the use for particle tracking was quite limited, having to rely on multiple of such detectors. To address this issue a new detector was developed - the **Multiwire Proportional Chamber (MWPC)**.

The *Multiwire Proportional Chamber* was introduced in 1968 by Charpak [23], whose contributions in the detector development granted him a Nobel Prize in Physics in 1992. This detector consists of a grid of equally separated anode wires, symmetrically sandwiched between two cathode planes, as observable in Figure 2.10. The cathodes may be composed of a wire grid, strips in PCB or of uniform conducting foil planes.
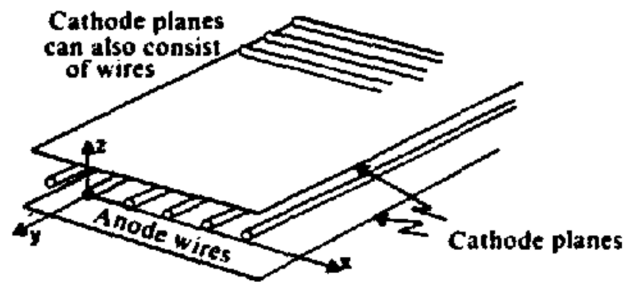
FIGURE 2.10: Configuration of a *MWPC*. From [23].

The configuration described originates an electric field as shown in Figure 2.11. It can be divided in two main regions: drift and multiplication. Most of the volume presents an uniform electric field, where the electrons will drift until closer to the anodes. At this point, the electrons are subjected to a high electric field, that increases closer to the anode wire, allowing for avalanche multiplication to occur. This process is similar to a singlewire *PIC*.

A great advantadge of *MWPC*s is that they are position sensitive and different methods of readout can be used [23, 24, 25]. For example, each anode wire can act as an independent detector, being connected to an amplification and shaping electronic circuit, allowing to determine the position of the interaction. Another example, that allows for 2D imaging, is the use of delay or resistive lines connecting the cathodes. For the case of resistive wires, the position on each wire is measured by the ratio of collected charge
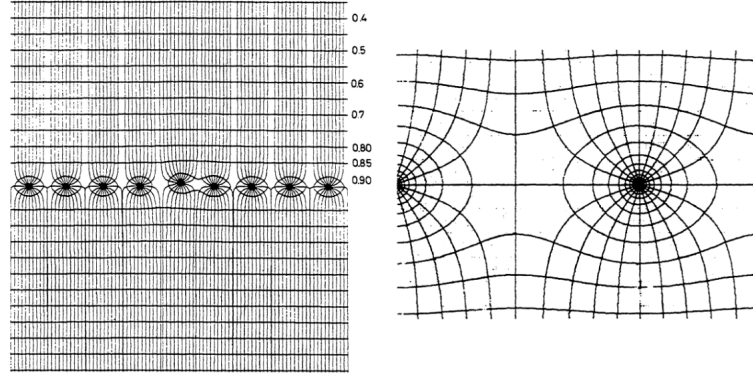
FIGURE 2.11: Left: Electric field equipotential lines and field lines in a *MWPC*. Right: Close representation of the electric field around the anode wires. From [24].

at the ends of the wires. When delay lines are used, the interval of time between the interaction and the detection of the signal represents the spatial coordinate.

Although, while *MWPC* have been widely used and remain effective in many applications, they present some limitations related to the their design. Their spatial resolution is limited by the wire spacing and they can experience saturation effects at high particle rates. Their production can be more labor-intensive and costly compared to modern alternatives. More recently a innovative detector concept was introduced - the **Micropattern Gaseous Detectors (MPGDs)**, relying on these modern alternatives for their fabrication, and offering improved performance and versatility.

Micropattern Gaseous Detectors were introduced in 1988 by the development of the Microstrip Gas Detector by Oed [26]. He introduced the application of microelectronics techniques, as photolithography, into the construction of gaseous detectors, leading to the development of more versatile and cost effective solutions compared to the already existing. Besides these advantages, they also present a better position resolution, high rate capability, multi-particle resolution and the potential for larger sensitive areas, when compared with the previous gaseous detectors [25, 22].

Several *MPGD*s have been developed in the last decades since the emergence of the Microstrip, such as the Micromesh Gaseous Structure and the **Gas Electron Multiplier (GEM)** [10, 22, 27]. Only *GEM*s will be discussed, for the purpose of this work.

In 1997, Sauli introduced the *GEM* [27]. Standard *GEM*s consist of a 50 µm thick

kapton foil, metal-coated on both sides and perforated with a high density of holes, in a hexagonal pattern. Each hole has a bi-conical shape, with an internal diameter of typically 50 µm and external of 70 µm, and are separated by 140 µm [28]. This configuration is visible in Figure 2.12.

The small structures allow for a good spatial and time resolution, of about 100 µm and 10 ns, making *GEM*s suitable for 2D imaging [10, 29].
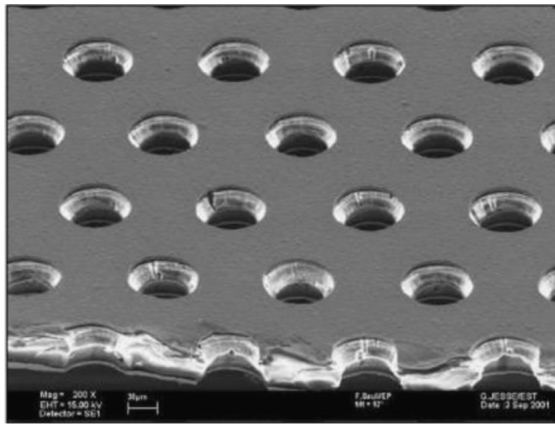
FIGURE 2.12: Microscope image of a typical *GEM* geometry. From [27].

When placed between two external electrodes (a drift and a charge collection electrode) the *GEM* is accordingly biased, originating an electric field, divided in three regions: an upper drift region, the multiplication region, inside the holes, as presented in Figure 2.13 and a lower induction region. The free electrons from the upper region drift towards the holes, thanks to a mild field between the drift electrode and the top surface of the *GEM* foil. In the holes, they are subjected to a high electric field, that induces electron avalanches. The electrons produced in the multiplication region are guided by electric field lines into a region below the *GEM* foil where they can be either collected by an electrode, or carry on to a second multiplication region, in case another *GEM* foil is placed below the first one. Due to the separation of the charge multiplication and collection, the signal readout is only originated by the electrons and not the ions. Therefore, it is possible to simplify and increase the speed of the processing electronics. This feature also reduces the risk of damaging the sensitive electronics, through discharges [25, 27].

In order to increase the overall gain, a cascade of *GEM* electrodes is commonly used since they can be operated with lower applied voltages which reduces the risk of
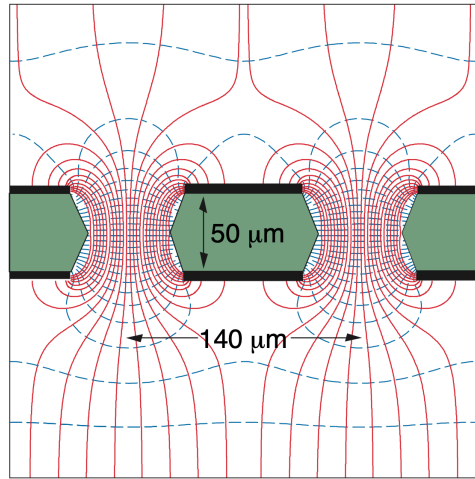
FIGURE 2.13: Electric field lines (solid red) and equipotentials (dashed blue) in a standard *GEM* detector. Typical dimensions are also presented. From [25].

discharges, given that the amplification is divided across the multiple *GEM* foils [27, 29]. A triple *GEM* detector is exemplified in Figure 2.14.
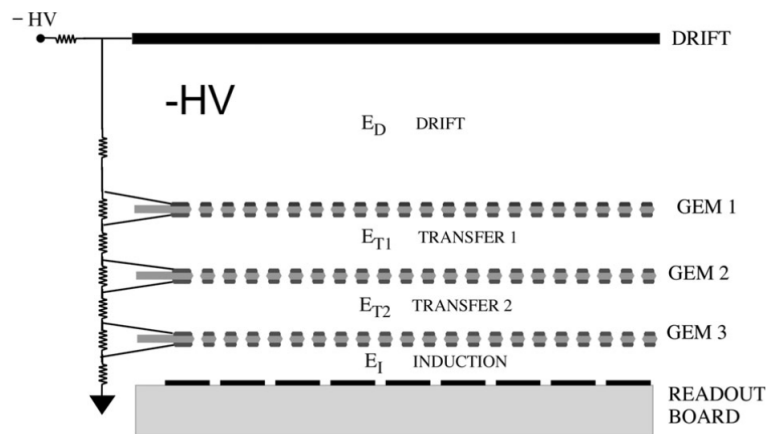
FIGURE 2.14: Scheme of a Triple *GEM* Detector. From [22].

Chapter 3

Single-Pixel Imaging

3.1 Concept

Single-Pixel Imaging (*SPI*) has its origins in the field of *Compressive Sensing* (*CS*), which is a mathematical theory that postulates that, under certain conditions, a signal or image can be reconstructed with a small number of measurements, more exactly below the Nyquist limit. The Nyquist limit states that, to accurately represent a signal, the sampling rate must be at least twice the highest frequency present in the signal [30]. More so, *SPI* is capable to form an image with only 3 main hardware components: a single-pixel detector, a light source and a spatial light modulator. The spatial light modulator is employed to project different pre-selected patterns onto a scene, strategically chosen from a sensing matrix, enabling effective image reconstruction. This has been proving to be revolutionary, since it allows for similar or higher image resolution, without the need to further increase the cost of the hardware, and making use of a sub-set of samples [31]. The mathematical formulation of *SPI* and *CS* will be presented, although in this work we did not use *CS*, because we have used low resolution *SPI*. *CS* is more effective and important only when imaging with high resolutions [5].

Mathematically, *CS* can initially be presented by the following:

$$x = \Psi\theta \tag{3.1}$$

where $x \in \mathbb{R}^{N \times 1}$ is the discrete signal and $\theta \in \mathbb{R}^{N \times 1}$ is the sparse vector that contains the x projections in the orthogonal basis, $\Psi \in \mathbb{R}^{N \times N}$ [9, 6].

Two important requirements in *CS* are sparsity and incoherence. A signal must be sparse, *i.e.*, few coefficients are able to represent the signal, and the sensing matrix, (Φ), must have low coherence with Ψ in order to form an N resolution image with M measurements, where $M < N$. In most applications, these are independent of the signal to be measured, resulting in a sampling process:

$$y = \Phi x = \Phi \Psi \theta = A \theta \tag{3.2}$$

where $y \in \mathbb{R}^{M \times 1}$ contains the sampled data projections using the sensing matrix (Φ) and A is the reconstruction matrix. In practical terms, Φ is projected onto the scene and A is used to reconstruct the final image [30].

Sensing Matrix

As mentioned, the sensing matrix chosen, must take into account the level of incoherence with the orthonormal basis. It has been proven that random patterns show the low incoherence required, but these introduce an additional degree of freedom, as they are not pre-designed matrices. Other options are Fourier, wavelet and Hadamard [32].

The matrix that we will be focusing on, that has already been demonstrated to be suitable for *SPI*, is the Hadamard transform matrix. It consists of a square matrix of only -1/1 values, obtained from the Walsh functions, orthogonal binary functions [33, 30]. This option stands out because of how simple it is to implement both in hardware and computationally, and, in this particular project, to design and print in a 3D printer.

The Hadamard matrices of first and second order are defined as [33]:

$$H_1 = \begin{bmatrix} 1 \end{bmatrix} \text{ and } H_2 = \begin{bmatrix} 1 & 1 \\ 1 & -1 \end{bmatrix} \tag{3.3}$$

From H_2, Natural ordering Hadamard transform matrix of order 2^k can be derived recursively with the following equation:

$$H_{2^k} = \begin{bmatrix} H_{2^{k-1}} & H_{2^{k-1}} \\ H_{2^{k-1}} & -H_{2^{k-1}} \end{bmatrix} = H_2 \otimes H_{2^{k-1}} \tag{3.4}$$

where k is an integer larger than 1 and $\otimes$ is the Kronecker product. The Kronecker product is an operation that combines two matrices by multiplying each element of one matrix with the entire other matrix, resulting in a larger matrix, more specifically with a size equal to product of the sizes of the two multiplied matrices [34]. Considering the Natural ordering Hadamard transform matrix of order 4, the process, step by step, would be the following:

$$H_4 = H_2 \otimes H_2 \tag{3.5}$$

Then,

$$H_4 = \begin{bmatrix} 1 & 1 \\ 1 & -1 \end{bmatrix} \otimes \begin{bmatrix} 1 & 1 \\ 1 & -1 \end{bmatrix} = \begin{bmatrix} 1 \times \begin{bmatrix} 1 & 1 \\ 1 & -1 \end{bmatrix} & 1 \times \begin{bmatrix} 1 & 1 \\ 1 & -1 \end{bmatrix} \\ 1 \times \begin{bmatrix} 1 & 1 \\ 1 & -1 \end{bmatrix} & -1 \times \begin{bmatrix} 1 & 1 \\ 1 & -1 \end{bmatrix} \end{bmatrix} = \begin{bmatrix} 1 & 1 & 1 & 1 \\ 1 & -1 & 1 & -1 \\ 1 & 1 & -1 & -1 \\ 1 & -1 & -1 & 1 \end{bmatrix} \tag{3.6}$$

As perceived, it is relatively simple to perform, even more computationally.

Each row of the Hadamard matrix can serve as a measurement mask, by reshaping its values into a 2D array. We start by dividing each row in 4 groups of 4 values, each will correspond to a column of a measuring mask [33]. In Figure 3.1, in blue, it is observable that row 5 corresponds to mask 5. In orange and red, it is shown how a group of 4 values is transformed into a column. By performing these steps on every row, the necessary set of maks is obtained.

So, the Hadamard matrix is used as a set of orthogonal basis patterns. By sequentially applying these measurement masks and capturing the corresponding measurements, it is possible to reconstruct an image or scene using computational algorithms.

As a way of reducing the background noise, differential Hadamard *SPI* has emerged. In this technique, in addition to using the set of masks mentioned, a measurement, m_{H^-}, is acquired with their inverse masks too. The value m_{H^-}, registered for each case is respectively subtracted from the value obtained with "original" masks, m_{H^+}, obtaining $x = m_{H^+} - m_{H^-}$. From this point, the reconstruction is carried out [33].
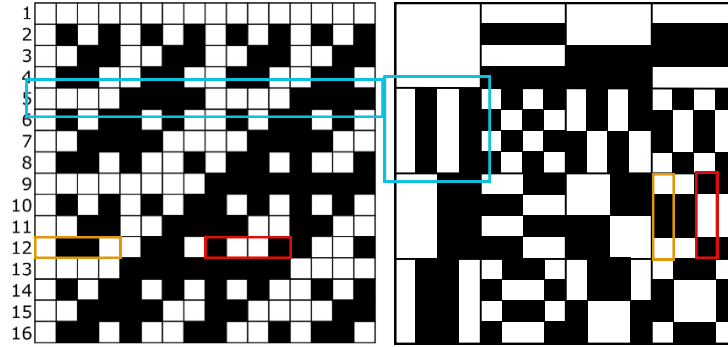
FIGURE 3.1: Hadamard matrix of order 16 in natural ordering with the corresponding reshaped patterns. Adapted from [5].

Computational Algorithm

In cases where transformation matrices have been applied, such as the Hadamard, the simplest way to reconstruct is to use their inverse transform.

Considering, a column matrix y of measured data, a column matrix x of target data and H, the Hadamard matrix, similar to what is described in the third step of equation 3.2 we can write the following:

$$\begin{bmatrix} x_1 \\ \vdots \\ x_n \end{bmatrix} = H^{-1} \begin{bmatrix} y_1 \\ \vdots \\ y_n \end{bmatrix} = \frac{1}{n} H \begin{bmatrix} y_1 \\ \vdots \\ y_n \end{bmatrix} \tag{3.7}$$

So, by transposing the Hadamard matrix, then multiplying it with the final measured values, y, we obtain x with the n final coefficients. One detail to note is that the inverse Hadamard matrix can be obtained by dividing the original Hadamard matrix by its dimension n, which further simplifies the computational work. By reshaping x into a $\sqrt{n} \times \sqrt{n}$ matrix and displaying it as 2D array, we will form the reconstructed image [32].

Using the Hadamard matrix obtained in the previous section (equation 3.6), the respective masks and the formula 3.7, a simple example for 4 pixels is given next. Considering the following:

Object　　　　**Hadamard matrix**　　　　**Masks**

FIGURE 3.2: Elements used for the example.

Each mask, presented on the right in Figure 3.2, is projected onto the object, presented on the left. Analytically, this procedure is presented by the first step in equation 3.2, obtaining the following coefficients:

$$y = \begin{bmatrix} 1 \\ -1 \\ -1 \\ 1 \end{bmatrix} \text{ or, when reshaped, } y = \begin{bmatrix} 1 & -1 \\ -1 & 1 \end{bmatrix} \tag{3.8}$$

Finally, the reconstruction formula can be applied resulting in:

$$x = H^{-1} \times y = \frac{1}{4} \begin{bmatrix} 1 & 1 & 1 & 1 \\ 1 & -1 & 1 & -1 \\ 1 & 1 & -1 & -1 \\ 1 & -1 & -1 & 1 \end{bmatrix} \times \begin{bmatrix} 1 \\ -1 \\ -1 \\ 1 \end{bmatrix} = \begin{bmatrix} 0 \\ 0 \\ 0 \\ 1 \end{bmatrix} \text{ or } x = \begin{bmatrix} 0 & 0 \\ 0 & 1 \end{bmatrix} \tag{3.9}$$

Other more complex and more effective algorithms can be used, both as a post-processing step after the reconstruction or as independent image reconstruction algorithms. Some of these include the use of optimization algorithms to reconstruct images with the minimum number of measurements, such as the *Total Variation Minimization by Augmented Lagrangian and Alternating Direction Algorithm* (*TVAL3*) and the *Nesterov's Algorithm* (*NESTA*) [5].

3.2 Experimental Setup

Regarding the setup used, there are two possible configurations to be analysed: *Structured Detection* (*SD*) and *Structured Illumination* (*SI*) [35, 5]. The main difference (concerning the hardware of the technique) between these two, is the sequence of the components. In *SI*, the X-ray source illuminates the masks, creating different patterns that consequently illuminate the sample or object. The transmitted intensities are then collected by the detector [35]. In *SD*, the illumination order is inverted, that is, the beam first reaches the object and only then it passes through the masks [35, 36]. Figures 3.3 and 3.4 represent both the structures for better comprehension from an optical perspective.
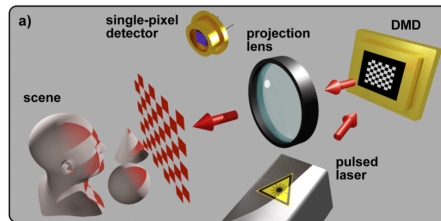
FIGURE 3.3: *Structured Illumination* (*SI*): in this case, the pulsed laser first illuminates a *Digital Mirror Device* (*DMD*), that is used to create the patterns, then illuminating the scene (object, as refered before). From [35].
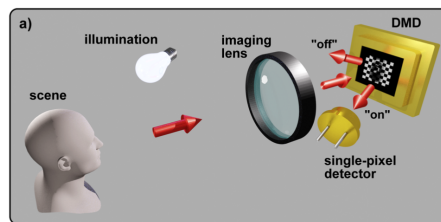
FIGURE 3.4: *Structured Detection* (*SD*): in this case, the light source is used to irradiate the scene, that consequently is imaged onto the *DMD*. From [35].

Given the fact that *SPI* is a relatively recent technique, with the main developments taking place over the past couple of decades [35], many studies are still being conducted with the objective of providing a better understanding of all the factors that contribute to the performance of such systems. The use of SPI to X-ray imaging has only started recently [35], which opens interesting research opportunities, yet to be explored.

Most of the studies with X-ray *SPI* are shown to use *SI* [7, 4, 37]. As proof of concept, regarding the possibility of accurate low flux X-ray imaging, [7] [37] performed experiments with similar setups.The experiments presented in [7] and [37] consist of similar setups, making use of a X-ray source, followed by an aperture to keep the beam perpendicular to the masks and object, blocking undesired photons from the surrounding areas. The main difference regarding these two approaches are related with the masks design. Zhang et al. [37] used randomly modulated patterns, while He et al. [7], opted for a specially designed Hadamard matrices. The object is placed in front of the masks, followed by the bucket detector. Both these papers were developed by the same research group dating of 2018 and 2020. In [37], a Princeton Instrument PIXIS-XB:1300 camera was used. The camera used has the capability of producing images with high resolution (1340x1300 pixels). In this case, the images obtained displayed a superior quality for projection imaging (a modality of medical X-ray imaging) for the same low flux. Improving the masks, provided an additional reduction on the exposure [7], minimizing the flux.

Alternatively, in 2021 Olbinado et al. [36] conducted a study aiming at proving that *SD* obtains better phase contrast and, therefore, better accuracy. In [36], the authors argue that the bucket detectors are not phase-contrast sensitive when the masks are set in front of the sample, staying unaffected by transparent sample configurations. A schematic of the setup used in [36] can be seen in Figure 3.5. In the setup presented, the authors made use of a coherent X-ray source, along with a special aluminum foam as test sample, transmission gratings as the near-orthogonal set of 1D masks, and a 1D bucket detector, in the order mentioned. By comparing the profiles in Figure 3.5, of a direct image detection (meaning, without the gratings) with a indirect phase-contrast ghost imaging, an almost identical behaviour was observed.

In [36], the authors concluded that the *SD* approach used had performed as expected, obtaining high definition images. When comparing with the *SI* method, it was possible to demonstrate the capability of obtaining enhanced images when using *SD* method.

Regarding the *SPI* systems configuration, these systems are formed mainly by three distinct elements [5]:

- single-pixel detector;

- light source;

- light modulator.
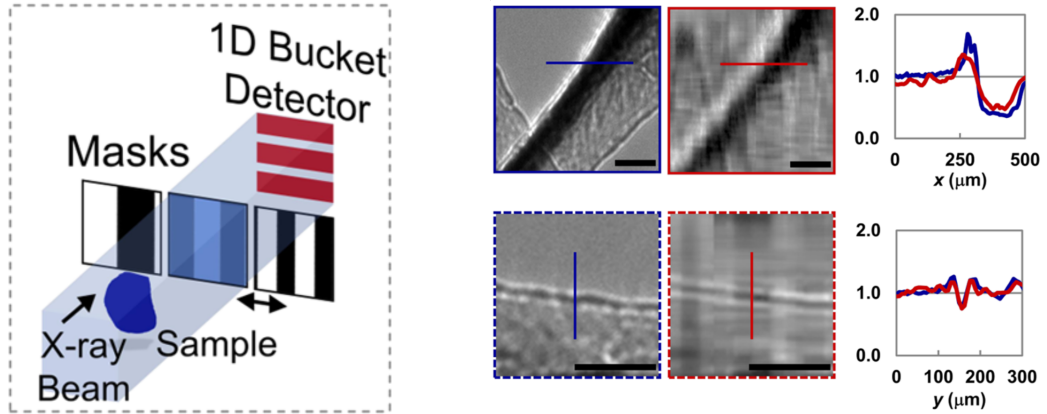
FIGURE 3.5: Left: Scheme of the experimental setup. Taken from [36]. Right: Above: Horizontal Line Profile. Below: Vertical Line Profile. In Red, is presented the direct imaging profile and in Blue, the indirect. From [36].

Starting by the light source, experimental demonstrations of X-ray *SPI* using synchrotron radiation from large accelerators have already been conducted [36, 38, 39]. Furthermore, the development of X-ray *SPI* was also made possible without the need for a highly coherent X-ray source. [30, 40, 41] A. Schori and S. Shwartz [39] performed an experiment using a tabletop incoherent X-ray tube source, trying to obtain increased sharpness images with ghost imaging. They measured the widths of two slits, of 10 μm and $100\mu m$, and compared their results with scanning electron microscopy, by representing the profiles of the slits (similar to what is presented in Figure 3.5 of the study made by Olbinado et al. [36]). Not only both the curves showed similar behaviour, but the ghost imaging measurements exhibited significantly better surface contrast. Most of the investigations following [7, 37], use tabletop sources, since this *SPI* attempt on reducing the total cost.

Some hypotheses are being investigated, concerning the light modulator. Zhang et al. [37] refer that *Digital Mirror Device*s (*DMD*s), frequently used in *SPI* and computational imaging systems [35], are unsuitable for X-ray radiation. In this case, a sheet of SiC sandpaper rotated by a step motor was chosen, creating random speckle patterns due to the sheet's grainy texture. In [39], copy paper is used with a similar function as in [37]. In more recent works, modulation masks are micro-manufactured, using light etching and lithography, in materials such as copper [7], gold [7, 36] and gadolinium oxide [42]. Olbinado et al. [36] chose a different strategy, by employing transmission gratings, arguing that these gratings for hard X-ray can be made using well-established

fabrication procedures.

Regarding the detector, in the past decade, for many applications in the visible wavelength spectrum, the development of *Charge-Coupled Devices* (*CCD*s) and *Complementary Metal-Oxide-Semiconductor*s (*CMOS*s) pixelated sensors has resulted in the advantages of low-cost, high-resolution imaging technologies. [35] However, at non-visible wavelengths, these are not feasible. *CCD* Imaging costs significantly more and requires substantially more processing time [7]. Other alternatives include a single avalanche photo-diode [39], a X-ray diode [7] and a *CCD* coupled with a scintillator [37].

3.3 Reconstruction Techniques

In this section, both the pattern fields used to selectively collect light in X-ray *SPI*, and the mathematical concepts that enable image reconstruction, are discussed.

3.3.1 Sensing Matrix

SPI initially employed random patterns for light modulation [32]. As referred in Section 3.2, the authors of [37] and [39] both used materials, such as sandpaper and copy paper, only relying on the granularity of such materials to form a non-orthogonal overcomplete set. As a result, retrieving information requires a high number of measurements and a lengthy data-acquisition time and not achieving the resolution of multi-pixelated techniques [32]. To overcome these limitations, sets of deterministic orthogonal patterns were applied, based on mathematical transforms, such as the Hadamard Transform and the Fourier Transform [32]. Studies of X-ray *SPI* applying these models have been conducted [7, 41].

As stated before in [7], authors have chosen Hadamard transform matrices as modulation scheme. They also experimented with sandpaper random patterns and were able to compare both. In Figure 3.6, are presented the images of the original object used (left) along with the images retrieved with sandpaper (center) and with Hadamard masks (right), for the same number of measurements, respectively. It is noticeably seen the better performance for the Hadamard case, where the letters are distinguishable from the background.

In [7], the *Contrast-to-Noise Ratio* (*CNR*) given by equation 3.10 was calculated, in order to provide additional quantitative information on the image quality. In this work, the authors concluded that for a relatively small number of measurements, the Hadamard masks obtain better resolution, but the *CNR* starts to worsen at a certain
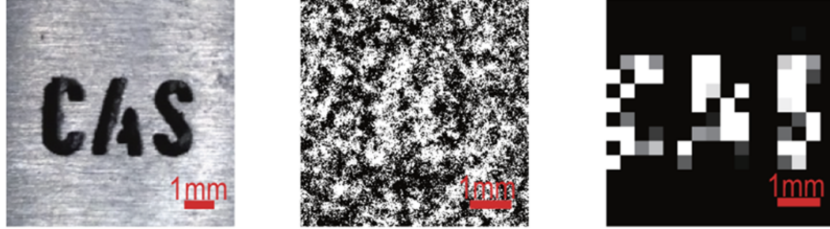
FIGURE 3.6: Left: Object used; Centre: Sandpaper X-ray Ghost Imaging retrieved after 128 exposures; Right: Hadamard X-ray Ghost Imaging retrieved after 128 exposures. From [7].

point. Furthermore, two hypotheses for this behaviour are presented: flaws on the masks caused by uneven electrochemical etching and the detector may not be sensitive enough to detect the smaller oscillations generated by finer patterns. To solve these, it is suggested replacing the detector and using more precise techniques to fabricate the masks.

$$CNR = \frac{\langle G_1 \rangle - \langle G_1 \rangle}{\sqrt{\sigma_1^2 + \sigma_0^2}} \tag{3.10}$$

where G_1 and G_0 are the ghost imaging values for the open and covered pixels, respectively, and $sigma_1^2$ and $sigma_0^2$ are the variances.

Alternatively, X-ray *SPI* using Fourier transform has also been reported [43, 41]. In [43], a *SD* Fourier *SPI* architecture was built in order to acquire radiography images for small animals. Although, the authors intend to use the same detector for fluorescence light, so they arrange the setup in way that the X-ray beam is converted into visible light. By employing this conversion of light, they were able to use *DMD*s as spatial light modulator. In [43], authors concluded that, the required anatomical data can be obtained using X-ray *SPI*, but at the cost of worsening the resolution and acquisition time, in particular when compared with conventional techniques. To overcome such limitations, it is suggested the implementation of deep learning algorithms.

3.3.2 Computational Algorithm

The generation of the actual image in *SPI* systems is achieved by correlating the intensity beams obtained in the detector using the different modulation patterns.

The most basic algorithms used are simple correlation functions, such as cross correlation [36] or the normalized second-order intensity correlation [39, 37]. In other cases, where mathematical transform matrices have been applied, it is common to use their inverse transform to perform the reconstruction [43, 32, 44, 41].

Furthermore, with the computational science growth, new computational algorithms are being developed [35]. Compressive sensing makes use of optimization algorithms to reconstruct images with the minimum number of measurements [9]. From this have emerged more complex algorithm, such as *TVAL3* and *NESTA*, that have shown better performance, both in regard of their execution speed, as in resolution, with a much smaller number of exposures [30]. For further improvement, deep learning approaches have started to be employed. Deep neural networks can efficiently detect the noisy features of a set of data, by being trained. This allows them to be used for image recovery, reducing the number of measurements [7, 45].

He et al. [7], using a X-ray *SPI* architecture, compares a compressive sensing algorithm, with *TVAL3* and with a deep learning algorithm developed within the research group, a compressible Hadamard plus multi-level wavelet convolutional neural network. As mentioned before, the contrast-to-noise ratio is calculated as measure of image quality and tested in three different objects. The first is presented in Figure 3.6, the second one is a metal gear with 14 teeth (Figure 3.7 in the left) and the third a gold semi-cylinder glued to a rectangular column (Figure 3.7 in the right). In the first case, it shows a CNR growing trend, from the first algorithm to the last, starting in 1.49 and ending in 2.43. In the second case, the CNR calculated were 0.6, 0.5 and 1.56. *TVAL3* displayed a worst performance then the other two algorithms, leading the authors to conclude that *TVAL3* fails to show finer details. As for the last object, only *TVAL3* and their algorithm was used, having obtained CNR values of 0.27 and 2.65, respectively, *TVAL3* showing again trouble with smaller structures. For better results, more training data should be provided for the deep learning algorithm.

3.4 Applications

Given the low cost and easy to operate setup [37], X-ray *SPI* has been showing a great potential for multiple applications. Being a low-dose radiation technique, makes an interesting technique for biomedical applications [38], since high dose can be harmful for soft tissues. Huang et al. [43] tested the ability of X-ray *SPI* to obtain the necessary anatomical information in small animals, to be more precise, in a female mouse bearing
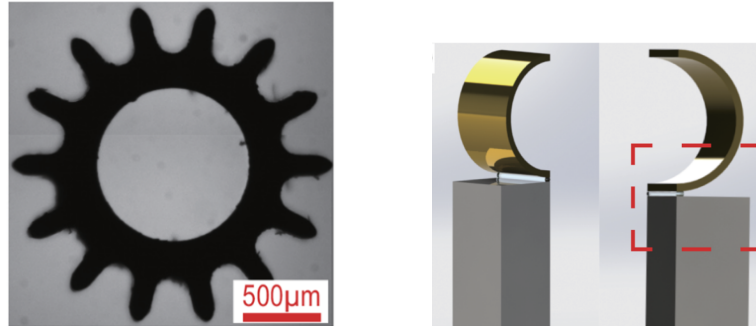
FIGURE 3.7: Objects used in [7]. Left: Metal Gear. Right: Gold semi-cylinder glued to a rectangular column.

tumor. The results demonstrated this imaging technique to be successful on obtaining this information. The authors actually design a multimodality system combining X-ray and fluorescence imaging in order to obtain both anatomical and molecular information, by merging two separate images. The outcome was compared with data captured with a *CMOS* camera and demonstrated to be in accordance.

Furthermore, the possibility of applying this in human medicine is of great interest, since the procedures used nowadays can be expensive and require specialized equipment and qualified personnel. Additionally, the radiation's potential hazard to human health is a factor key. In [46], Kingston et al. show several numerical simulations with different approaches to ghost tomography. In this work, different strategies regarding dose distribution are explored, reducing noise and the set of masks to be chosen. The authors concluded that masks that form an orthogonal basis are more effective than random masks. Besides that in [46], authors affirm cross-correlation algorithm may be inadequate and suggest the use of machine learning and artificial intelligence to achieve better reconstruction and to perform more data processing. A final answer is not given to the question if this technique can reduce radiation dose, which would be an important advantage in sensitive biological specimens [37]. Other suggestion is to employ phase-contrast ghost imaging, that since this article was written has already been demonstrated [36].

X-ray *SPI* has also been proven to be useful for secure inspections where baggage control is needed, while keeping private most of the imaging [47]. In [47], Gilbert et al. make use of blind compressive sensing, using a single-pixel architecture to capture information on specific items without never forming a full image. For this study, it is considered both a robust and secure inspection system, being reliable, with the capacity to identify similar objects and detect variations, while the specific features remain private

to the individual, being those the location, shape and size of the object. In this case, the robustness was tested by adding white noise and verifying the ability to distinguish between the true object and similar ones. In [47], authors demonstrate that the method used shows strong capability to distinguish until noise level of 1%.

Other applications of this technique can be found in material diagnosis [7], internal structure inspection of products and components in industry, as to perform the quality control while they are being manufactured [7]. The application to archaeology and art conservation and restoration was studied [35]. X-ray *SPI* shows potential to be applied to all the purposes where conventional X-ray techniques are used.

3.5 Concluding remarks

There are many potential applications for X-ray imaging, leading to a growing interest in developing this technique. More and more studies are being conducted in order to achieve low-cost setups with high resolution and efficiency. In table 3.1, is displayed a brief summary of the most recent studies using *SPI*.

In the present work, Hadamard matrices will be used, as they have displayed good results in previous works [7]. A key aspect for the present research is that the modulation scheme not be grey scaled, as is the case with Fourier matrices. The goal in this work will be to employ fast prototyping techniques such as 3D printing and CAD to develop the materials and structures to be used in the development of the experimental system. In this case, patterns of 0s and 1s are a simple solution, easy to design and print with the needed precision.

TABLE 3.1: Summary of studies showing the evolution of X-ray *SPI* and the testing of different features.

Study	Setup	Sensing Matrix	Algorithm	Objectives
Pelliccia et al. (2016)	Structured Illumination	Random pattern	Second Order Correlation	Feasibility of X-ray imaging
Schori and Schwartz (2017)	Structured Illumination	Random pattern	Second Order Correlation	Feasibility of tabletop sources architecture
Zhang et al. (2018)	Structured Illumination	Random pattern	Second Order Correlation	Feasibility of X-ray imaging with low dose radiation
He et al. (2020)	Structured Illumination	Random pattern & Hadamard transform	TVAL3 & Deep Learning	Resolution improvement with better reconstruction techniques
Olbinado et al. (2021)	Structured Detection	Set of vertical lines	Cross Correlation	Higher phase contrast and accuracy with *SD*
Huang et al. (2022)	Structured Detection	Fourier transform	Inverse Fourier transform	Acquire multimodality images with *SD* Fourier *SPI* (proved the feasibility of Fourier X-ray *SPI*)

Chapter 4

Development of a setup with a Single-Pixel Detector

This chapter provides an overview of the development of the system employed in the present study, being divided in three parts. We start by describing the experimental setup and mention some considerations regarding the setup in general. The two following sections focus on the development of the set of masks and the design and assembly of the detector.

In Section 4.4, many considerations are described until reaching the final 3D-printed set of masks, taking into account both simulation and experimental results. In Section 4.5, a full characterization of the detector is done.

For the definition of the experimental setup, we considered both the requirements from the point of view of the detector, in our case, a triple *Gas Electron Multiplier* (*GEM*) detector and the standard *Single-Pixel Imaging* (*SPI*) setup, bearing in mind the fact that we used X-ray radiation.

A single pixel camera based on *Structured Detection* (*SD*) was developed to test the concept of X-ray *SPI*. The designed camera was composed by three main components/parts: the set of masks that contain the different patterns, a triple *GEM* detector, with the electronics associated, and an X-Ray tube. The *Data Acquisition* (*DAQ*) system used comprised of three elements: a *Charge-Sensitive Amplifier* (*CSA*), a Shaping Amplifier and an *Analog-to-Digital Converter* (*ADC*), connected to a computer with the *DAQ* and analysis. In Figure 4.1, a scheme of the setup is presented. Numbers 1, 2 and 3 refer to the *CSA*, the Shaping Amplifier and the *ADC*, respectively. To operate the detector, a high-voltage power supply is needed to bias the internal structures (cathode and *GEM*s).
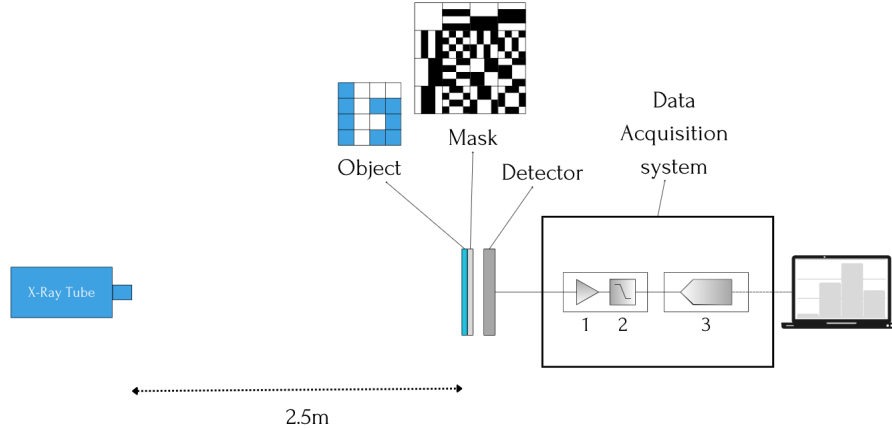
FIGURE 4.1: Schematics of the experimental setup.

The next sections specify the components used with more detail. A description of a ^{55}Fe source is given too, since one is used for some tests with the detector. The information regarding the detector and the masks are described in Sections 4.4 and 4.5, given that, for these two components, more tests and evaluation was necessary.

4.1 X-ray Sources

In a ^{55}Fe source, a radioactive source, the X-rays are generated through electron capture. The atom nucleus decays into ^{55}Mn leaving the atom in an excited state. Upon de-excitation, the atom emits X-rays with two possible energies: a Kα of 5.9 keV or a Kβ of 6.4 keV, with a probability ratio of 100 to 20.

As for the X-ray tube, the model used in this work was the Mini-X XRay Tube from AMPTEK [48]. It includes a Mini-X X-ray tube module with a built-in high voltage supply, and can be configured by the supplier software (Figure 4.2). It was necessary to place the X-ray tube at a distance large enough for the beam to be considered perpendicular to the detector surface. This way the photons would hit the object, the mask and the detector in the same position.

In the Table 4.1, some specifications related to the X-ray tube can be seen. The high voltage and the current can be defined by the user in the software as shown in Figure 4.2. Throughout the entire work, the lowest settings were used, 10 kV and 5 µA, since we wanted to reduce dose as much as possible and, by increasing this, a charging up in the detector could happen (more information in Section 4.5.4).
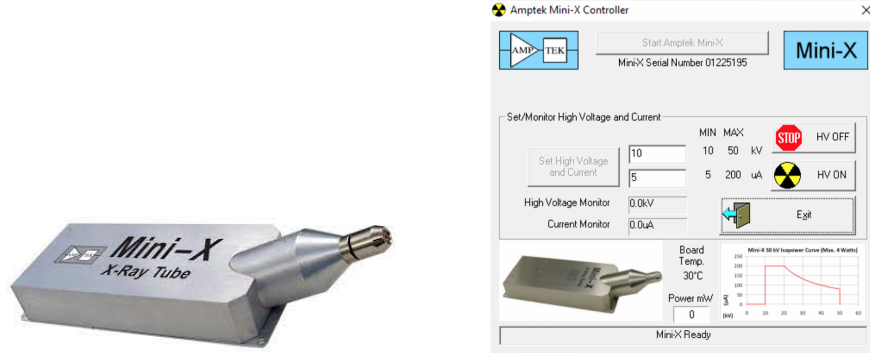
FIGURE 4.2: Left: Mini-X2 X-ray tube module and the Mini-X2 Controller. From [48]. Right: User interface of the Mini-X2 Software [48].

TABLE 4.1: Specifications of the X-ray Tube. (The target material refers to the anode hit by the fast electrons.)

Input Voltage	5 VDC (USB)
High Voltage	10 - 50 kV
Filament Current	5 - 200 µA
Target Material	Gold

In the scope of this work, it is important to have a detailed information regarding the emission spectrum of the X-ray tube, as it will be necessary for the performance evaluation of the *SPI* setup used. See Figure 4.3.
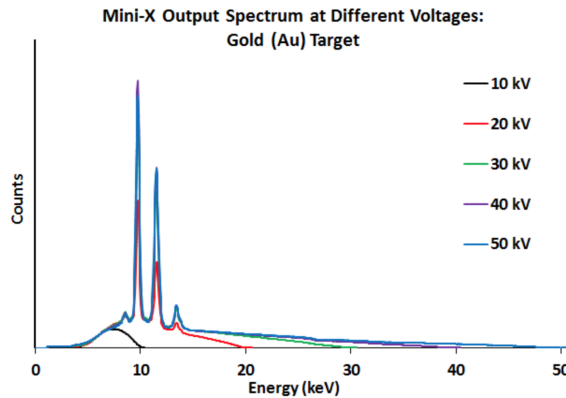
FIGURE 4.3: Output Spectrum for the Mini-X. From [48].

4.2 Detector

The detector used was a 10×10 cm^2 triple *GEM* detector as presented in Figure 4.4. Each *GEM* foil has 70 μm holes separated by 140 μm. It has a 3 mm drift gap, 2 mm transfer gaps and 1.5 mm induction gap. The chamber is continuously filled with Ar/CO_2 (70/30) at a rate of 6 L h^{-1} through the gas in/outlets. It has a 50 μm thick entrance window made of kapton.
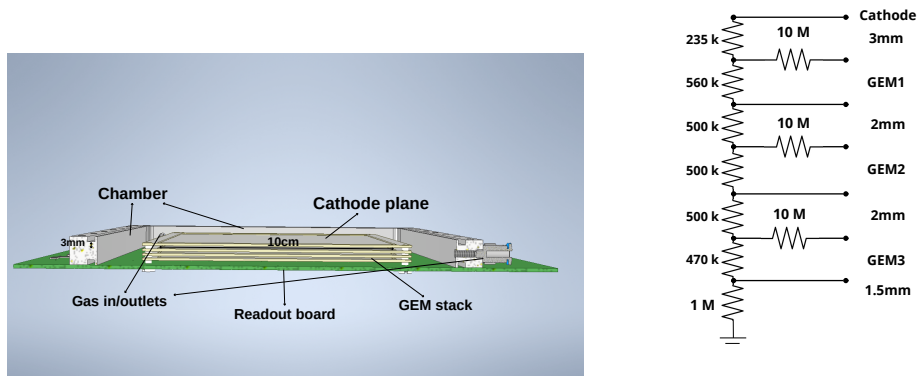
FIGURE 4.4: Left: Detector schematics. Right: Voltage divider (the units of the values are Ω).

As explained in Section 2.2.2, a voltage is applied in each electrode, originating an electric field, which allows for charge multiplication. For this work, the detector was chosen to function with an effective gain of approximately 10^4. From Figure 4.28, the voltage to be applied is 2830 V. This corresponds to voltages across the GEM foils of around 400 V, which is the typical voltage used in such detectors [27]. The slightly higher voltage in the first *GEM* provides a larger signal immediately after the collection of the primary cloud, promoting a better energy resolution, as the consequences of the statistical fluctuations introduced by the other *GEM* foils are reduced. On the other hand, the last *GEM* foil, which is more susceptible to electrical discharges because of the much larger number of electrons has a slightly lower voltage, that can improve the operational stability of the detector [49]. Considering the voltage divider presented on Figure 4.4 (right side), 2830 V corresponds to approximately 760 μA through the tension divider. That results in 600 V cm^{-1} drift field, 2 kV cm^{-1} field in the transfer gaps and 5 kV cm^{-1} field in the induction gap.

4.3   Components

4.3.1   High Voltage Supply

The model used for the high voltage supply was the CAEN Module N8034 [50]. Only one of the 8 HV channels in the module was used. This module has a voltage and current range that fitted our needs, plus it had the possibility to be controlled through its LCD touchscreen or remotely by its associated software, using USB or Ethernet. In the Table 4.2, some specifications related to the High Voltage Supply can be seen.
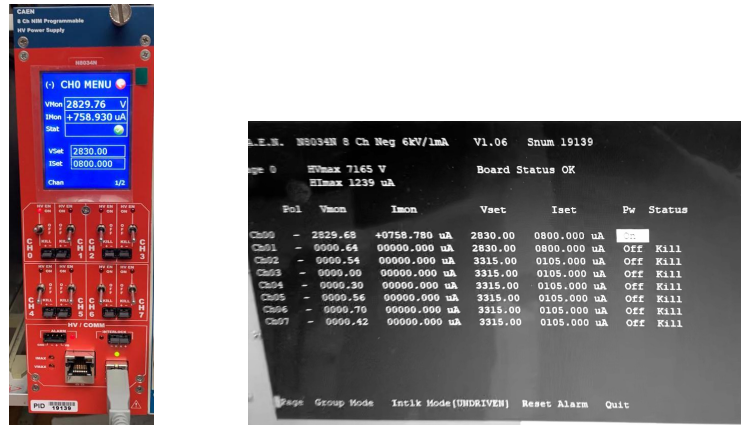
FIGURE 4.5: High Voltage Supply and interface software. Left: CAEN Module N8034. Right: Interface of the CAEN Software.

TABLE 4.2: Specifications of the High Voltage Supply.

Output Channels	8 independent channels
Max Output Voltage	6 kV
Max Output Current	1 mA

The settings applied were 2830 V and a maximum of 800 µA, considering the current of 760 µA, as already mentioned.

4.3.2   *Charge-Sensitive Amplifier*

Its function is to convert the electrical charge generated by the radiation into a voltage signal. It integrates the charge of the signal and converts it into a voltage step, as shown in Figure 4.6 [51, 52]. This is usually done using a capacitor.

The model used was an ORTEC 142B pre-amplifier [53], as presented in Figure 4.7.
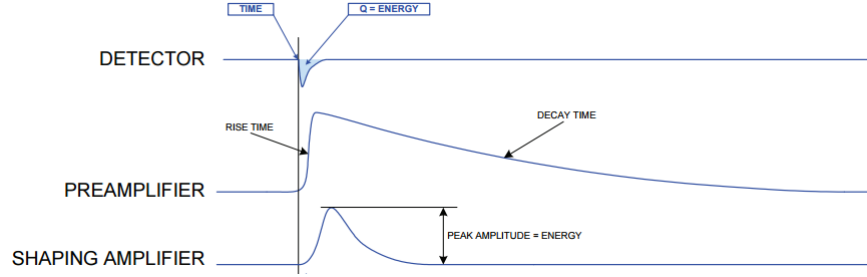
FIGURE 4.6: Pulse integration and shaping through the electronic circuit. From [51].

FIGURE 4.7: ORTEC 142B pre-amplifier.

4.3.3 Shaping Amplifier

For the shaping amplifier, the Canberra Model 2111 Timing Filter Amplifier, shown in Figure 4.8, [54] was used. This was connected to the *CSA* and, as the name indicates, its function is to shape the signal integrated by the *CSA*, shaping it into a Gaussian, in order to prevent event pile-up and to transform the peak into a readable signal for the *ADC* [51, 52].

After adjustment, the following features, shown in table 4.3, were the ones set throughout the rest of the work.

TABLE 4.3: Specifications of the Shaping Amplifier.

Fine Gain	1.25
Coarse Gain	10
Differentiate (nS)	500
Integrate (nS)	50
Polarity	Non-inverted

FIGURE 4.8: Model 2111 Timing Filter Amplifier.

4.3.4 *Analog-to-Digital Converter*

The *ADC* used was the Canberra ADC 8715 module [55]. This component is responsible for the digitization of the signal, transforming the signal amplitude into a number that could be used to fill a histogram of the energy distribution in the detector as presented in Figure 4.9. The ADC Reader software was developed in the IEAP and allowed for pre-definition of the acquisition time and many parameters for a fast initial analysis of the data, such as two markers to obtain the current count value in two specific positions and the integral in between.
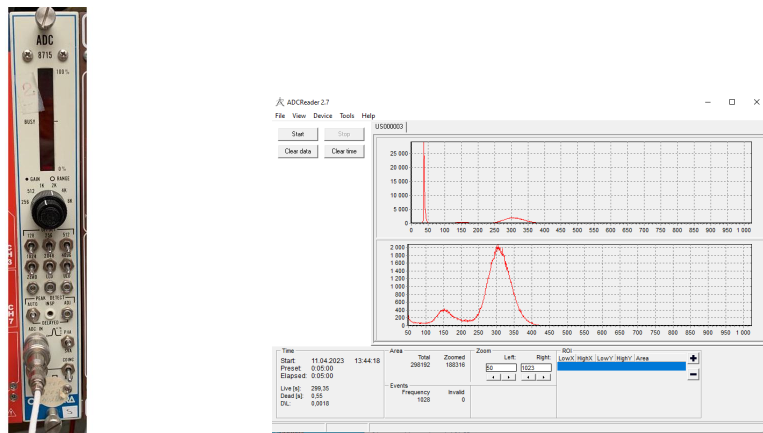
FIGURE 4.9: *Analog-to-Digital Converter*. Left: Canberra ADC 8715 module. Right: User interface of the ADCReader.

4.3.5 Gas supply

The detector was filled with an Ar/CO2 (70/30) mixture at an open flow of $6\,\mathrm{L\,h^{-1}}$ that assured an exchange of ten times the chamber's volume per hour. The flow was controlled by commercial mass flow controllers.
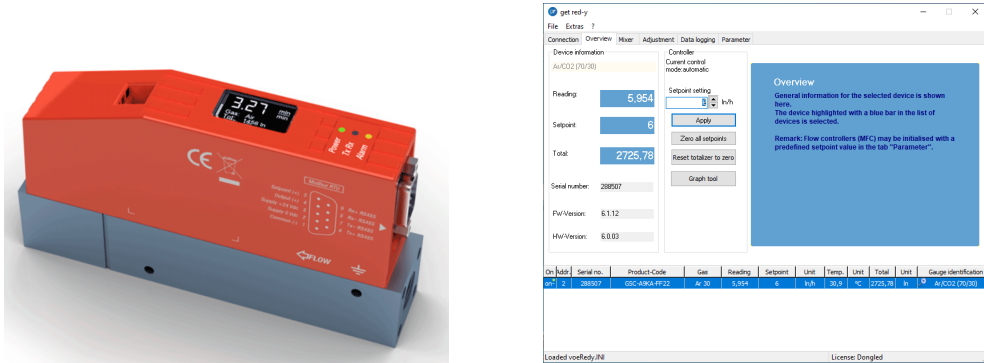
FIGURE 4.10: Mass flow controller and software. Left: Voegtling red-y smart controller GSC. From [56]. Right: Interface of the get red-y Software.

4.4 Mask Studies

In an initial state of this project, the X-ray *SPI* concept was tested computationally, performing simulations in *GEANT4*. First, a simplified version of the system was designed (see Figure 4.11). This was done in order to test both different materials of the masks and different thicknesses, as a way of finding the optimal operating point.
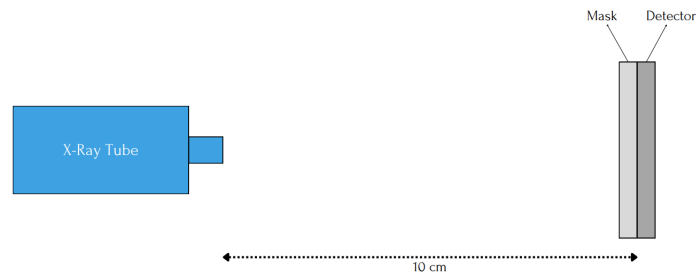
FIGURE 4.11: Setup for the first type of simulations (not at scale)

As indicated in Figure 4.11, the blue rectangle to the left represents the X-ray Tube. In our case, a "General Particle Source" (a type of source already defined in *GEANT*4) of γ particles, with the energy spectrum emitted by the X-Ray Tube was defined. The

source was set as point source with isotropic angular distribution and at a distance of 10 cm from the detector, as shown in Figure 4.11. Regarding the detector, it was defined as a 10×10 cm^2 active area with a 2 mm absorption region. The gas mixture selected was Argon-Carbon Dioxide at atmospheric pressure ($Ar - CO_2$ (70/30)). For the mask, an area of 10×10 cm^2 was defined, with a variable thickness and material in order to study different cases.

Tables 4.4 and 4.5 summarize the tests performed. It is important to note the first four materials mentioned in the table, as they all are filaments available for 3D printing [57]. These were studied in order to pre-select the best option before printing the set of masks for the final prototype. The last two materials are commonly used for radiation shielding, serving as a comparison in the analysis of their performance.

TABLE 4.4: Different materials tested.

Materials	Density ($g\,cm^2$)	Chemical Formula
Polylactic Acid filament	1.24	$C_3H_4O_2$
Polyethylene Terephthalate Glycol filament	1.27	$C_{10}H_8O_4$
Polyvinyl Butyral filament	1.10	$C_8H_{14}O_2$
Acrylonitrile Styrene Acrylate filament	1.07	$C_{18}H_3NO_2$
Copper	8.96	Cu
Aluminium	2.70	Al

TABLE 4.5: Different thicknesses tested.

Thickness (mm)	
Filaments	Metals
0.5	0.005
1	0.01
2	0.02
3	0.05
4	0.1
5	

4.4.1 Material Selection

The transmission of X-rays through different materials and thicknesses was studied and the transmission ratio was obtained. This ratio was obtained by dividing, the number of events detected in the active volume of the detector with the mask, by the number of

entries detected in the active volume of the detector when the material of the mask is set to vacuum.
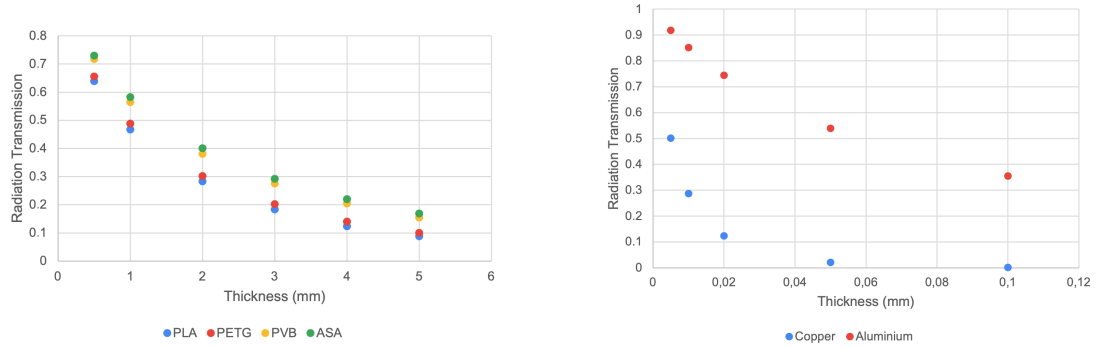
FIGURE 4.12: Radiation transmission as function of the material and thickness. Left: Polimers. Right: Metals.

The plots obtained are presented in Figure 4.12. What is expected is that higher density and atomic number materials, or in other words, higher electronic density, with the same thickness, will have smaller transmission. From Table 4.4, we can observe that the results in simulations are mostly consistent with that. When comparing the first plot, it is clear that the *Polylactic Acid Filament* (*PLA*) has a lower transmission. This is particularly important as contrast in such *SPI* will be highly dependent on how much radiation passes through the material. In this case, we are interested in materials with high density and atomic number. Even though metals provide a better performance, one of the objectives of this project was to test this technique with masks fabricated by 3D printing. Having all of the above taken into account, and the fact that *PLA* was already available at the moment in the laboratory, this material was the chosen one.

For selecting a thickness, it was considered the percentage of blocked radiation and the quantity of material used while printing. It is clear from the plots above (Figure 4.12), that increasing thickness results in more X-Rays being blocked in an exponential trend, as is expected by the Beer-Lambert's law, shown in equation 2.3.

Since 5 mm offered good performance and the amount of material required was still manageable, both in terms of cost and dimension, the decision was made to produce 5 mm *PLA* masks.

4.4.2 Mask Thickness

4.4.2.1 Detector Response

To obtain the expected response of the detector to different thicknesses of *PLA*, an online tool (available at [58]) for X-ray interaction with matter was used. It uses tables of cross sections of X-ray interactions and calculates it considering the law of attenuation as mentioned in 2.1.2. This software allows to choose a material (solid or gas), define some of their characteristics (see Figure 4.13) and choose its thickness or path length. Then, it is possible to select a range for the photon energy and it returns a transmission spectrum and the respective data file.

FIGURE 4.13: Software interface. The features that the software requires us to define can be seen: chemical formula, pressure/density, temperature and path length/thickness. Above: Software for gases. Below: Software for solids.

For our work, we considered the following setup in Figure 4.14. In that figure, it is possible to see the different setup components. A simplified configuration was used to provide an initial estimate of the detector response. In the image, is possible to see the an air gap, resulting from the spacing between the source and the mask, followed by the *PLA* component, followed by a simplified configuration of the detector (that includes a $50\,\mu\text{m}$ kapton window and an active volume with a $2.5\,\text{mm}$ thickness (Ar/CO_2) (70/30)).

The transmission spectrum for each material and thickness/path length was obtained. With that, it was possible to calculate the absorption of the detector with a structure of *PLA* in front (equation 4.1). For this formula, the product of the transmission for the
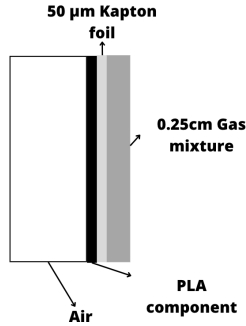
FIGURE 4.14: Setup for the simulation of the response of the detector. (not at scale)

layers before the detector is done and then it is multiplied by the probability of being absorbed in the detector. For the calculation of the absorption, the gases in the gas mixture are considered to be separated, one after the other, provided that their partial pressure is defined accordingly with the proportion in the mixture. If the radiation is absorbed in the first gas, it "stops" and it is no longer available for the second gas. It is also important to note that their order is irrelevant, since the result will be the same.

$$A_{detector} = T_{PLA} \times T_{air} \times T_{window} \times ((1 - T_{Ar}) + T_{Ar}(1 - T_{CO_2})) \Rightarrow \qquad (4.1)$$

$$A_{detector} = T_{PLA} \times T_{air} \times T_{window} \times (1 - T_{Ar}T_{CO_2}) \qquad (4.2)$$

where A stands for absorption and T for transmission. The final spectrum is presented in Figure 4.15. This allows to characterize the detector response as a function of the incident energy, allowing to understand which energies is the detector more efficient, for each thickness. For larger thicknesses, the peak position will be farther from the origin, because the lower energy photons will be absorbed by the *PLA* mask.

The *PLA* masks work as a shield for the X-rays and the lower limit depends on the thickness (considering everything else to remain the same). A lower threshold is detected for approximately $3\,\text{keV}$, due to the air gap and the kapton window, that do not allow for lower energies photons to reach the detector. Evidently, the probability of radiation of lower energies reaching the detector increases with decreasing thickness.
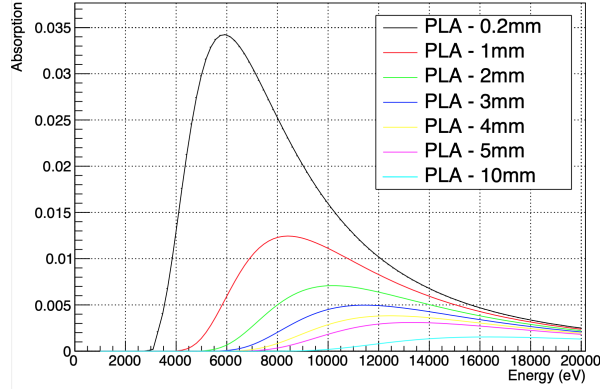
FIGURE 4.15: Plot of the absorption of the detector for different *PLA* thicknesses. The air gap was considered to have a thickness of 10 cm.

4.4.2.2 Experimental Test

To complement this work, a simple experiment was carried out. With the system already assembled, and using a ^{55}Fe source, two *PLA* structures were designed, allowing to test the transmission with different thicknesses.

In Figure 4.16 at the left, we have a photo of the package containing the ^{55}Fe source used. In the centre and the right, we have a photo of one of the structures used. We can observe its circular shape, with a total diameter of 5.6cm so that the 5cm source fits inside. In order to reproduce the position of the source, it also features salient edges. Except for the four holes, which have varying thicknesses, the inside portion of the mask has a thickness of 5mm. As we rotate the iron source inside the mask, those four holes align with the iron source's aperture. The mask has rectangular incisions on the edges that serve as a guide to align the source with the respective *PLA* thickness, so that it is easily verified the setup conditions and avoid possible misalignments (Figure 4.16).

The masks tested for the following thicknesses are presented in Table 4.6. Both have a region with 0 mm, to perform a quick calibration if needed. As all masks will have a base layer with 0.2 mm thickness, as will be discussed in the next section, we have included a region with that thickness.

So, for each thickness, 25 minutes of data were collected, obtaining the counts vs *ADC* channels spectra, in a *.txt* file. To each spectrum, using *Root software*, a gaussian fit was adjusted, registering its parameters, such as the centroid, sigma and amplitude.

FIGURE 4.16: Source and masks used in the thickness test. Left: ^{55}Fe source used in the laboratory. From the top and from the bottom. Centre: Picture of the mask from the top. Right: Picture of the mask from the side.

TABLE 4.6: Different thicknesses studied.

Mask 1	Mask 2
0 mm	0 mm
0.2 mm	1 mm
2 mm	3 mm
4 mm	5 mm

The spectra obtained for different mask thicknesses are shown in 4.17. The red lines represent the fitted Gaussians to each case. There are three different measurements for 0 mm, because it was performed one for each mask and then one at the end of the experiment, in order to see if the conditions had changed throughout the day.
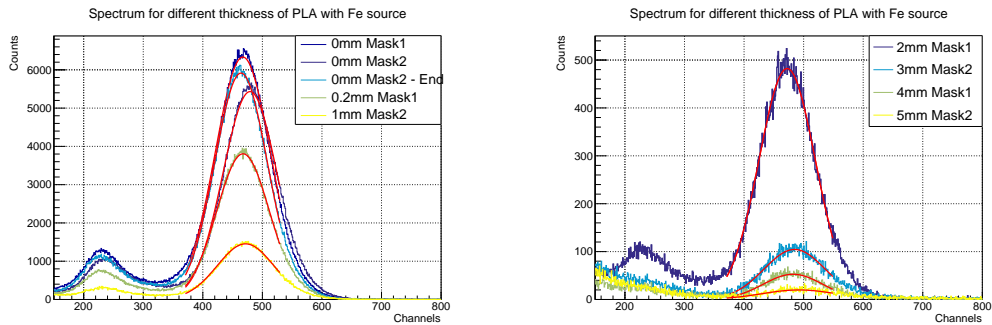
FIGURE 4.17: Energy spectra for different thicknesses of *PLA* with ^{55}Fe source.

In order to determine the total number of counts for each thickness, the integral of the curve was computed using the same limits in all cases. The transmission ratio was then calculated by dividing each number of counts by the counts with 0 mm, similar to what was done in the simulations. In Figure 4.18, the final plot is presented.
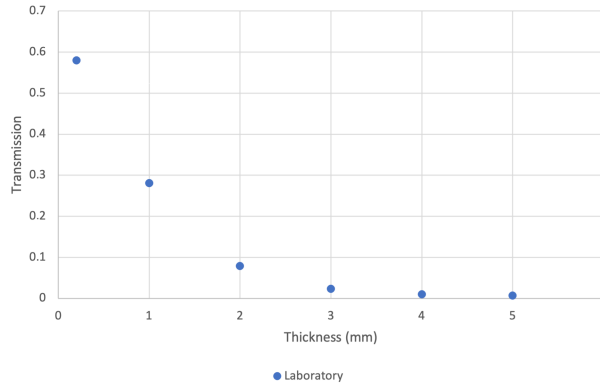
FIGURE 4.18: Transmission ratio as function of the thickness for *PLA*.

It is clear that the behavior of the curve resembles that seen in simulations, although, the values are different. The reasons for that are that his study was performed with the iron source and not with the X-ray tube, because it is easier and more cost-effective to design and print masks for the ^{55}Fe source, than for the X-ray tube, given that in that case it would be needed to cover the entire surface of the detector. Also the fact that, in the case for 0 mm, in the simulation it was considered vacuum, and in the laboratory, that was not possible. Although, to obtain a direct comparison to the experimental results, a simulation similar to the ones described, only changing the source to a $10 \times 10 \text{ cm}^2$ squared 5.9 keV mono-energetic source, and for *PLA* masks, was performed. The combined results are presented in Figure 4.19 (left side).

Given the difference in behaviour of the two curves, it was concluded that the 3D printer probably printed the *PLA* masks with a density lower than what expected, even with the selected 100% infill. Considering that, an estimated correction thickness factor was obtained by observation of the plot on the left in Figure 4.19. So, by comparing the two curves, we can say that the transmission for 1 mm in the simulation and 2 mm in the laboratory are approximately the same, and the same verifies for 2 mm in the simulation and 4 mm in the laboratory. Therefore, a factor of 2 can be approximately assumed. In practical terms, the thickness used in the laboratory must be double the thickness in the simulation to correct the difference in density and obtain the same level
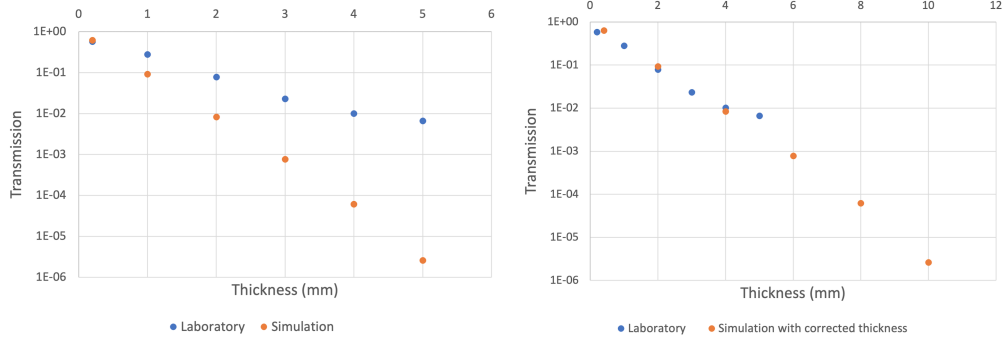
FIGURE 4.19: Logarithmic plot for the transmission with a ^{55}Fe source, or 5.9 keV. Left: combined plot of the simulation and experimental test. Right: original data for the experimental test and simulation data with a corrected thickness.

of transmission in both simulation and laboratory. This correction is exemplified in the right plot of Figure 4.19, where we can observe that the curves overlap.

A consideration that should be made is that the contribution of air can be neglected in the printed masks, and the most significant contribution comes from the fact that the filling is not at 100%. From table 4.7, we can note that the absorption in the air does not exceed 1.5% for the range of thicknesses studied, deducing that the inclusion of air within the structure does not significantly alter the results; also, for this reason, and for the sake of simplicity, we chose to modify only the thickness in the correction presented in Figure 4.19 (right side).

TABLE 4.7: Transmission values in different air paths with a temperature of 295 K and a pressure of 760 Torr obtained with the software available at [58].

Thickness (mm)	Transmission
0.2	0.99942
1	0.99711
2	0.99423
3	0.99135
4	0.98849
5	0.98563

4.4.3 Mask Set and Target Construction

Using *Autodesk Inventor*, each Hadamard mask was drawn as in Figure 3.1, plus their inverse versions. In Figure 4.20, two examples of the masks designed are shown. As in the first part of the simulations, they are $10\,\mathrm{cm} \times 10\,\mathrm{cm}$. From here on, the thickness was already defined as $5\,\mathrm{mm}$, based on the results obtained in the Section 4.4.1. In this case, some special features were included, such as the hole in each corner and the extended limits on each mask. Both features were designed to fix and correctly place the object in the experimental part.
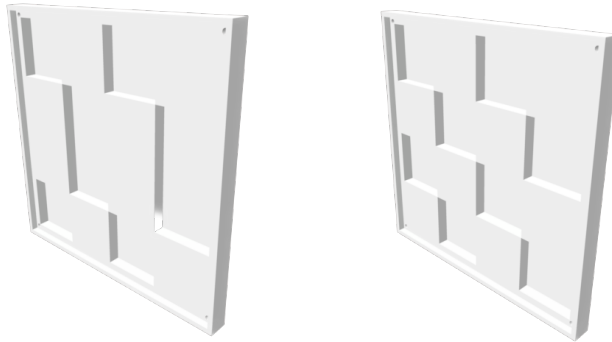
FIGURE 4.20: Examples of the designed Hadamard masks.

Following this, an object for the initial tests was designed and constructed using the same technique and material. The chosen object was the letter F due its asymmetry, that allows for a better perception of the orientation of the axis. Also, it is easy to draw with only 16 pixels.
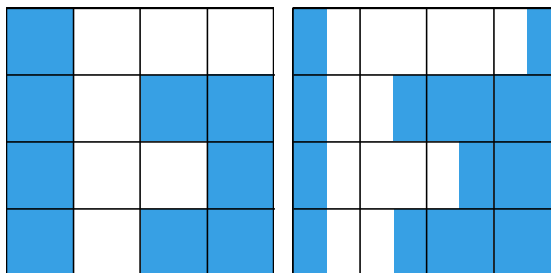
FIGURE 4.21: Scheme of the position of the letter F. Left: Used aligned sample position. Right: Misaligned sample position.

In Figure 4.21, on the left side, it is presented a scheme of the sample used where the white part is opened and the blue part is covered with *PLA*. The lines on both images are

a visual aid for the division of the pixels. On the right side of the figure, a representation for better comprehension on why the letter needs to be aligned with the pixels is shown. In the letter, it is possible to see that the pixels that are half covered will detect half the events than the totally opened ones. As a result, those pixels will appear with half the intensity as only half of the area will be exposed to radiation. Thus, making the object imperceptible, as presented in Figure 4.22.
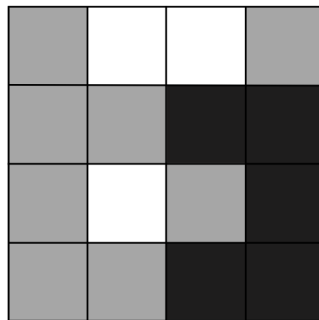
FIGURE 4.22: Scheme of the expected result of the measurement with the object F Misaligned with the pixels as shown in Figure 4.21 (right side).

Before printing the final masks some tests were made to assess the 3D printer. The model used was the Original Prusa i3 MK1. To print out the pieces, it is necessary to first, export the file from *Autodesk Inventor* as an STL file and after, import it to *PrusaSlicer* software, where there are different parameters to choose from, before printing. Having that ready, the file is exported as a G-Code file and uploaded to a SD card, that is compatible with the printer.

The limitations found with the 3D printing were mainly related with that since the printing is performed vertically, all the printed parts need a supporting structure. The fact that the joint corners of the inner structures of the masks have an infinitesimal thickness cannot be reproduced without separation of the pixels. Figure 4.23 shows a detail were a small separation between corners can be seen. The solution found for that was to add, a small 200 μm base layer, at the bottom of all masks, which is the minimum limit of the printer, minimizing the X-ray photon absorption.

Another important limitation is related to the infill of the masks, which theoretically should be 100% compact, but it is not possible with this 3D printer. Although, after investigation of the different infills available in the software [57], to obtain a density
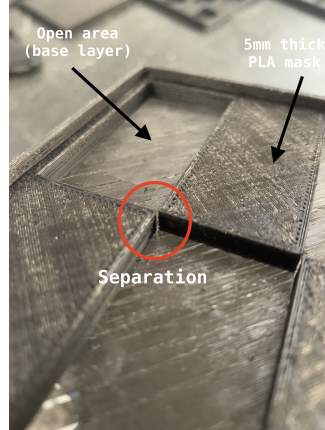
FIGURE 4.23: Detailed image of the masks showing the connection in the vertex and the base layer of 200 µm.

of close to 100%, we chose a rectilinear infill, that "zig-zag" across the whole layer. In Figure 4.23, it is observable the pattern created while printing.

Finally, it was decided to add borders along the masks' perimeter in order to fix and support the object to be imaged through X-rays. These measure 2 mm in thickness and 3 mm in height. A 2 mm diameter hole was made in each corner for the same reason so that a screw could fit and help in the positioning of the structure in the detector, while enabling some alignment with the detector window. For visual perception, this is shown in Figure 4.24.

Regarding the object, it was printed as presented in Figure 4.21, with 5 mm thickness and made of PLA. The sample also includes 2 mm side borders and corners that are squarely cut off to accommodate the screw. The object is presented in Figure 4.24.

In conclusion, the final result is shown in Figure 4.25, both the positive and the negative masks. Only a smaller set of masks was to be printed as some of the masks can be obtained by rotating masks from the set chosen. These other masks are obtained by simply changing the orientation of the initial set, thus avoiding the use of additional material. For this reason, only 11 masks were printed instead of the total set of 16.

4.5 Detector Assembly and Characterization

As mentioned before, the detector used was a 10×10 cm^2 triple *GEM* detector as presented in Figure 4.4.
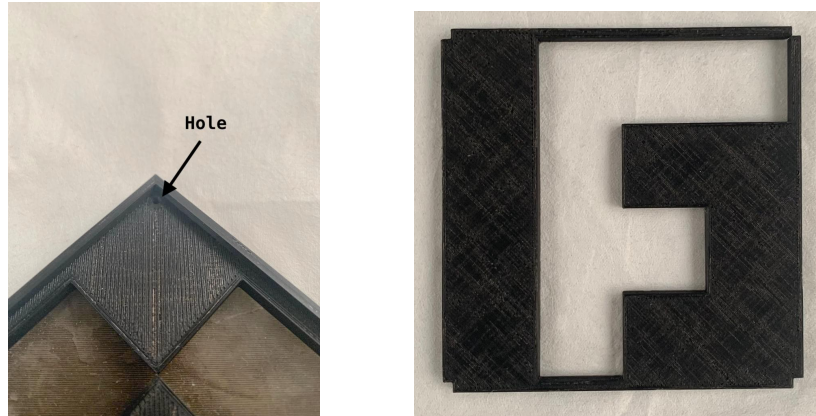
FIGURE 4.24: Left: Detail of the corner of a mask, showing both hole and the borders. Right: Printed sample with the letter F.

FIGURE 4.25: Hadamard set of masks. Left: Positive. Right: Negative.

In order to do its characterization, some features were determined. In an initial simulation test, the detector response was calculated to different features changed. Next, experimentally, its gain and energy resolution was determined. Finally, some tests were performed regarding its uniformity in area and in time.

4.5.1 Calculation of the Detector Response

Using the online software [58] already mentioned, the expected response of the detector in relation to X-ray poly-energetic radiation was determined. A similar setup is considered, as presented in Figure 4.14.

Previously, the feature changed was the thickness of PLA. In this part, two different studies were performed. One, by altering the concentrations of the gas mixture and other

by changing the path length of the air, or in practical terms by modifying the distance between the source and the detector. The spectra obtained are presented in Figure 4.26 and the different cases are indicated in each legend.
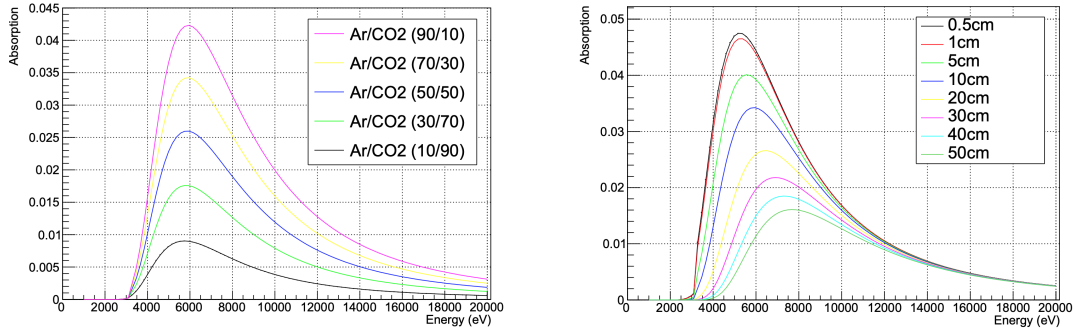
FIGURE 4.26: Left: Plot of the absorption of the detector for different gas mixture concentrations. Air path length of $10\,\text{cm}$ and *PLA* thickness of $0.2\,\text{mm}$. Right: Plot of the absorption of the detector for different air path lengths. Gas mixture of Ar/CO_2 (70/30) and *PLA* thickness of $0.2\,\text{mm}$.

On the left in Figure 4.26, the effect of different gas mixture concentrations can be seen. By changing the concentrations, the relative amount of each gas will change. Since argon has a Z higher than carbon or oxygen, if the percentage of argon is increased (decreasing the concentration of carbon dioxide), the absorption in the gas mixture is expected to increase. This is observed in the plot.

On the right in Figure 4.26, it is observable the effect on the number of photons detected, with the distance between the source and the detector, considering a normal air filled room. For shorter air path lengths, the count rate is evidently much greater, since less beams are deviated or absorbed by particles. Plus, for larger air paths lengths, we can observe that the photons that reach the detector are the higher energetic, that have a lower absorption in the detector.

4.5.2 Energy Resolution

The energy resolution was determined for different values of voltage applied, with a ^{55}Fe source, by the calculation of the *Full Width at Half Maximum* (*FWHM*). This aspect is obtained by performing $2.355 \times \sigma$, where σ is obtained from the Gaussian fit parameters. The values obtained are presented in Figure 4.27.
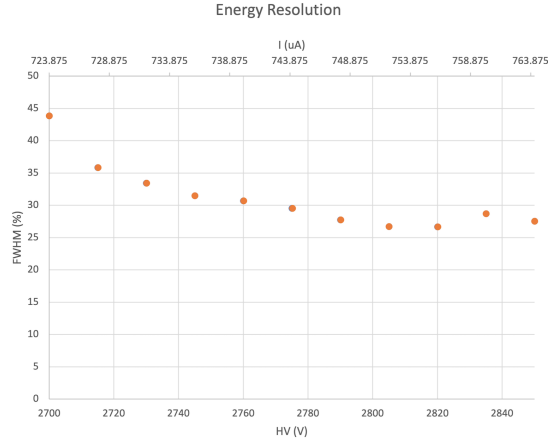
FIGURE 4.27: Energy resolution of the detector as a function of the applied voltage.

Is important to note that this study was done mainly in order to characterize the detector, because for this work only the number of events detected, and not their energy, was necessary. We can see that, initially the energy resolution improves, since the gain of the detector increases and, consequently there is an improvement in signal-to-noise ratio. At the end, since the drift field increases, primary electrons start to get lost in the top of the first *GEM* surface.

4.5.3 Detector Gain

Another important characteristic of a detector is its gain, which was tested with a ^{55}Fe source and calculating the following:

$$G = \frac{Q_f}{Q_p} = \frac{f_{cal}(M)}{q_e \times E_{photon}/\text{W-value}} \tag{4.3}$$

where Q_f is the charge detected, Q_p is the primary charge, M is the mean *ADC* value of the ^{55}Fe peak, f_{cal} is the electronics calibration function, q_e is the electron charge, E_{photon} is the ^{55}Fe photon energy and W-value is the mean energy necessary to create an ion pair in Ar/CO_2 (70/30). The electronics calibration function was obtained by using a waveform generator connected to inject a pulse signal and determining the tension before and after the amplification circuit. Then, the calculation of the charge was done for each input tension, using the preamplifier's capacitance, and the peak centroid in the *ADC* was determined. With that, it was possible to plot the input charge as function of

the mean *ADC* value. The results can be observed in Figure 4.28, where an exponential trend is observed, as expected.
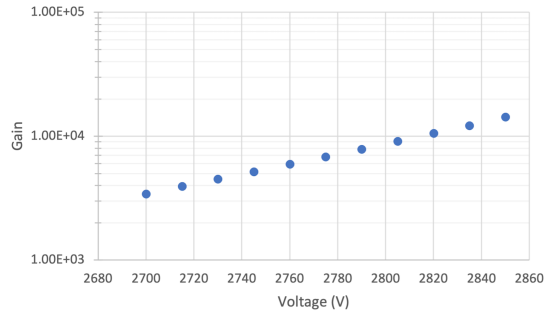
FIGURE 4.28: Logarithmic plot of the gain as a function of the applied voltage for the ^{55}Fe source.

4.5.4 Detector Uniformity

Uniformity in area

In order to obtain the best results, it is important that the entire active area of the detector is uniform, in terms of energy resolution and gain. Non-conformity in the holes and *GEM* foils can lead to non-uniformity [29]. Thus a test experiment was designed. Three *PLA* masks were developed as shown in Figure 4.29. Each mask has the same dimensions as the ones designed for the single-pixel measurements. These masks have only one 25×25 mm^2 pixel open, this way, it is possible to evaluate one pixel at a time. Only three were necessary, since by rotating them it is possible to examine all cases, and more material would be saved this way.
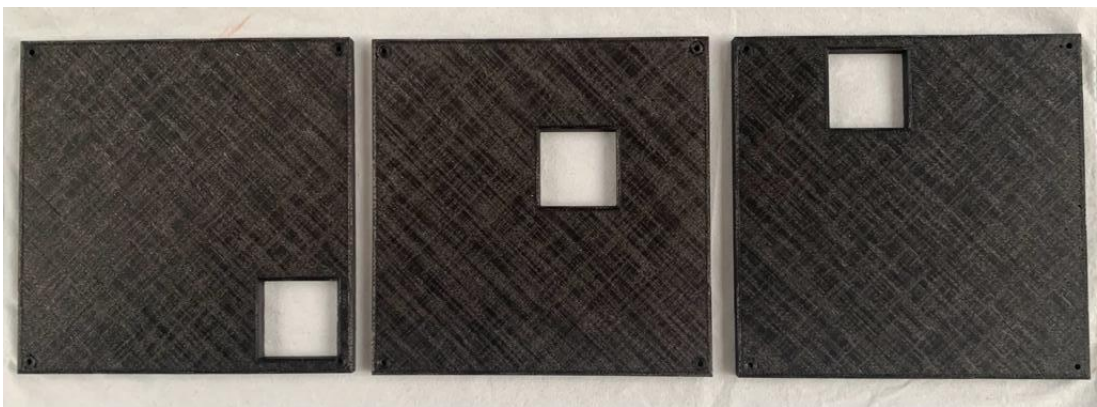
FIGURE 4.29: Masks design for the uniformity test.

Using the setup mentioned in the previous chapter, one minute of data was acquired for each pixel. The data acquired is presented in Figures 4.30 and 4.31.
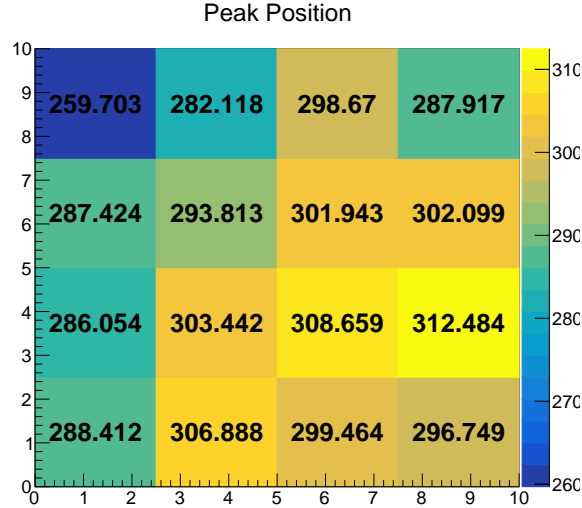
FIGURE 4.30: 2D Histogram of the position of the peak formed in the spectrum for the whole active area representing the colour map regarding the uniformity of the detector, with the X-ray tube. The values displayed are the position of the peak obtained.

For the evaluation of the gain, it was opted not to refer to absolute gain, we only show a relative variation of the peak position in the spectrum, which already gives us an idea on what the gain is (see Equation 4.3), since it makes the calculations simpler and in the final imaging measurements the absolute gain is not obtained. To calculate the peak position, a Gaussian fit is applied to each spectrum, using the built-in function from *Root* software. After iterative methods, it returns these three parameters: amplitude, centroid and sigma. So, in Figure 4.30, the values of the centroid are presented for each pixel. It is possible to denote a disparity towards the top left corner. This can be due to some problem in the assembly of the detector, leaving the cathode or *GEM*s not aligned and parallel. The standard deviation was calculated with equation 4.4 and divided by the average in order to characterize the non uniformity. The value obtained was of 13.2 %, a value inside the standard for this type of detectors [29].

$$dev = \sqrt{\frac{\sum(pp - \overline{pp})^2}{N}}$$
(4.4)

where *dev* stands for standard deviation, *pp* for peak position, $\overline{pp}$ for mean peak position and *N* for the number of measurements, 16 in this case.
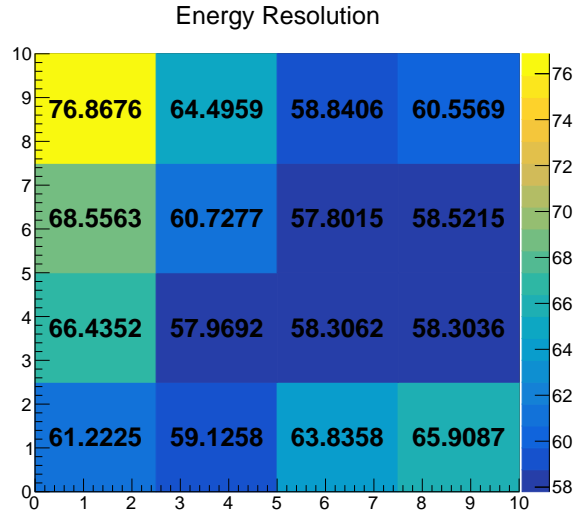
FIGURE 4.31: 2D Histogram of the energy resolution for the whole active area representing the colour map regarding the uniformity of the detector, with the X-ray tube. The values displayed are the energy resolution obtained.

A similar study was done for the energy resolution. From the data, we can see the same behaviour as for the peak position. Although, a more thorough study about this characteristic can be done, since the acquisition time was not that large.

Gain uniformity over time

While taking measurements with the masks, using the X-ray tube, we noticed a variation in gain and energy resolution. We noticed that thorough-out the day, while using the X-ray tube, the position of the peak would decrease. In the next day, the gain had been reestablished and the process repeated itself.

In order to accurately analyse that variation, one minute measurements were collected, with the X-ray tube permanently on and always with the same mask, to remove the effect of the different patterns. Initially, data was collected each 10 min, and then was changed to 5 min, when the signal peak started to approach the noise peak. This study was performed during 90 min, since, at that moment, it became difficult to distinguish the noise peak from the signal peak in the spectrum formed.

After the 90 minutes, the X-ray tube was turned off. To also evaluate the "recovery", the X-ray tube was turned on during one minute each hour and data was collected, after the study described before. The results are presented in Figure 4.32.
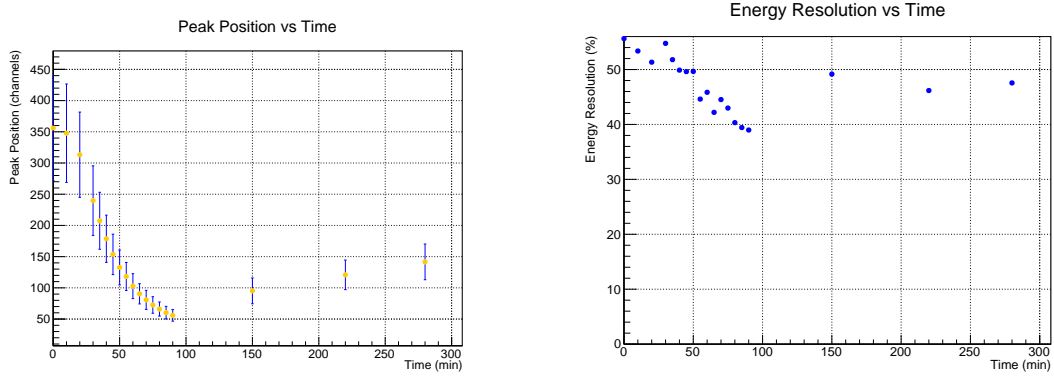
FIGURE 4.32: Long term operation stability of the detector. Left: Peak position. Right: Energy Resolution.

The effect is clearly observed, specially in Figure 4.32, on the left. We believe this is a charging up effect [59], due to the intensity of the X-ray tube used, since this was not observed when the ^{55}Fe source was used through-out the day. In the plot, we can also see a linear recovery behaviour with the X-ray off, which explains why in the next day, the peak position was reestablished.

As for the energy resolution, a similar behaviour is observed, although the data is much more scattered than in the plot for the peak position. Once again, a more complete study can be performed on this parameter.

Chapter 5

Results and Discussion

5.1 Simulation Results

As part of proof of concept, a more accurate setup was modelled. The masks, the sample and the "detector", developed as in the first part of the simulations, are assembled, in *Autodesk Inventor*. Figure 5.1 shows the setup as seen in *Autodesk Inventor*.
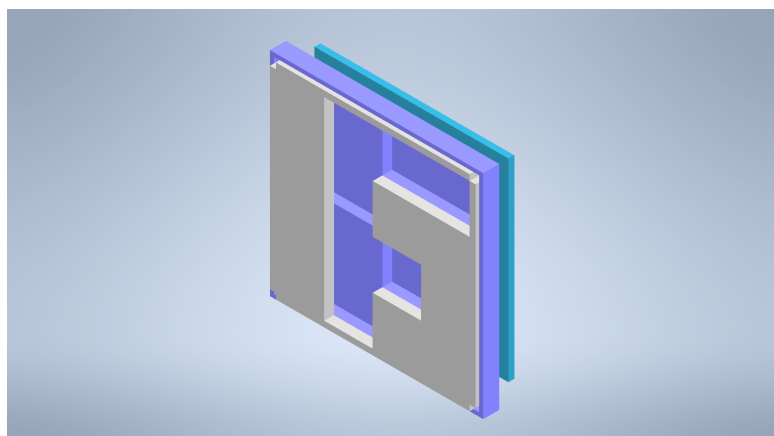
FIGURE 5.1: Example of assembly of the setup for the simulations.

A 10×10 cm^2 square uniformly emitting parallel X-rays was defined as the particle source, centered accordingly with the rest of the setup and 30 mm away from the detector. Unlike the first time, we now defined a flat source so the X-rays would irradiate the whole area with parallel photons, since now the position is also important. The setup as presented in Figure 5.2, similar to the one in Figure 4.1, was imported to *GEANT4* using a framework developed in the IEAP, that imports the GDML (Geometry Description Markup Language) files converted from the CAD design into *GEANT4* to perform the simulations.
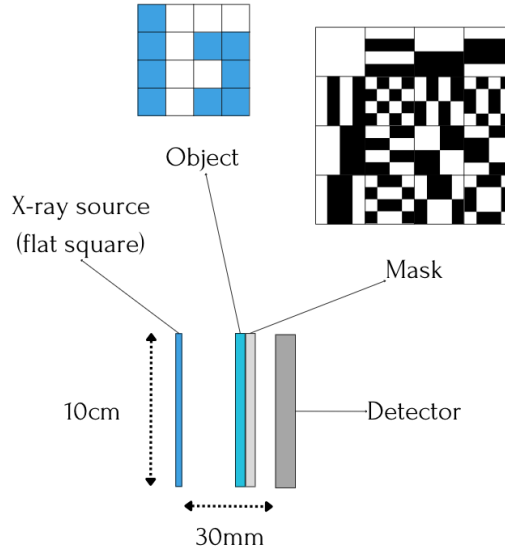
FIGURE 5.2: Setup for the final simulations.

We used monoenergetic beams at 6, 10, and 15 keV, as well as rectangular beams with a width of 2 keV ranging from 2 to 14 keV. The spectrum of the X-ray tube was also used. In addition, a separate set of simulations was performed changing the thickness of the masks for 1, 2, 3 and 4 mm and using the spectrum of the X-ray tube.

Having the setup prepared, it is possible to simulate the measurements for the 16 Hadamard masks, plus their inverse, and, finally, obtain the counts to reconstruct the image of the object.

After obtaining the data for all the patterns, we determined the number of events for each case, using *Root software*, since the files were already in *.root* format. Even though it wasn't required, we plotted a 2D histogram for each mask since it was interesting to be able to see the image from the "perspective" of the detector. The result is shown in Figure 5.3.

By applying the formula discussed in Section 3.1, we were able to reconstruct the final image. In order to evaluate in a more quantitative way, we also calculated the *Contrast-to-Noise Ratio* (*CNR*) with the following equation:

$$CNR = \frac{signal}{\sqrt{\sigma_s^2 + \sigma_b^2}} = \frac{\overline{w} - \overline{d}}{\sqrt{\sigma_w^2 + \sigma_d^2}} \qquad (5.1)$$
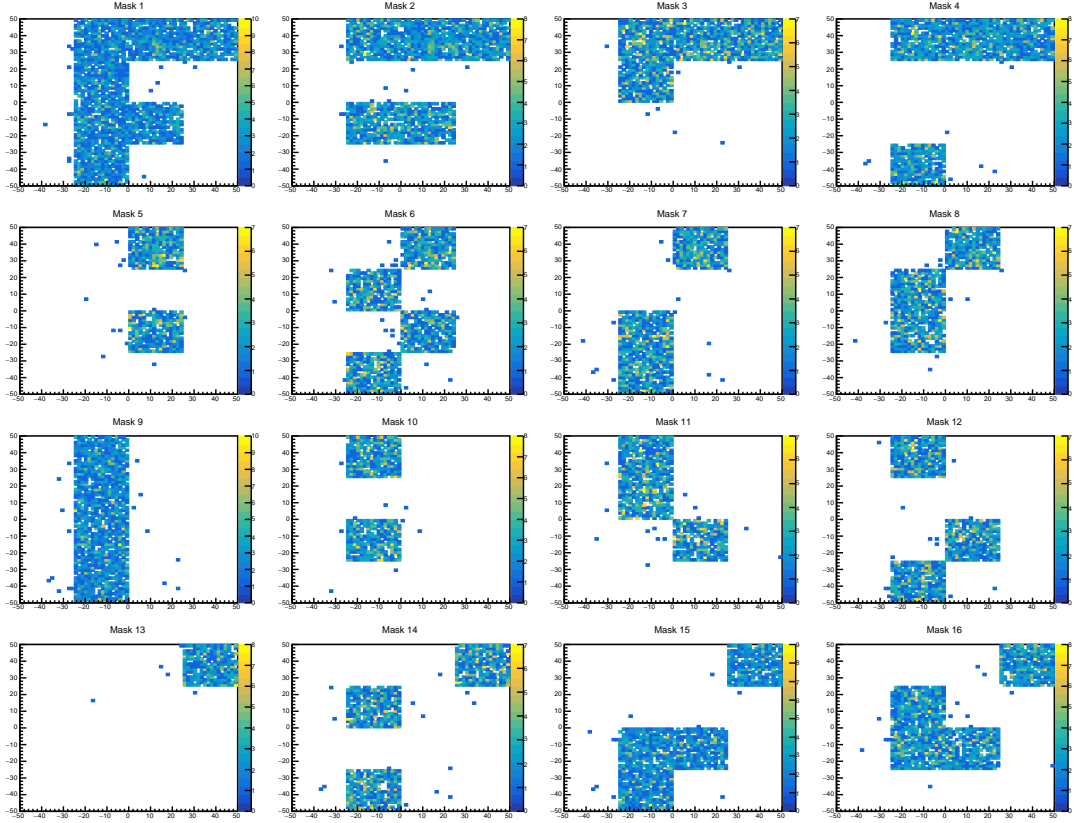
FIGURE 5.3: 2D histograms obtained for each mask. Example for a monoenergetic source of 6 keV and 5 mm *Polylactic Acid Filament* (*PLA*) masks.

where σ_s^2 and σ_b^2 are the variances of the signal and the background, respectively and w and b, stand for white and dark pixel. For our work, we considered that the background noise was the values on the covered parts, or the dark pixels, and the signal was the signal were the open pixels, or the white parts. All the values, were first normalized.

Both the images and the *CNR* values obtained are presented in the following subsections. In the end of presenting the different cases, Figures 5.8 and 5.11 sums up the results in two plots.

5.1.1 Spectrum of the X-ray Tube

As an initial test, the source was defined to have the spectrum of the X-ray tube, as it happens in the experimental part.
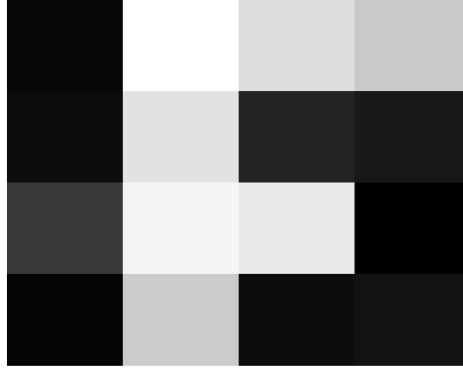
FIGURE 5.4: Reconstructed image for the spectrum of the X-ray tube.

TABLE 5.1: *CNR* value obtained for the spectrum of the X-ray tube.

	CNR
X-ray Tube Spectrum	8.2100

We can see that the letter F formed in the image (Figure 5.4) is clearly noticeable. Although, there many grey pixels, both in the uncovered part as in the covered part, which explains the value of the *CNR* (table 5.1). Since, as will be shown in the experimental part, we didn't actually use the complete spectrum for the reconstruction of the image, further research was required.

5.1.2 Mono-energetic Source

In order to form an idea on what energies worked better for this technique, we also tested with different mono-energetic sources.

TABLE 5.2: *CNR* values obtained for mono-energetic sources.

	CNR
6 keV	24.8902
10 keV	10.5320
15 keV	1.7958

We can do an initial assessment of the images (Figure 5.5) and postulate that lower energies work better, which makes sense since, in the pixels that are covered, more

(A) Reconstructed image for 6 keV.

(B) Reconstructed image for 10 keV.

(C) Reconstructed image for 15 keV.
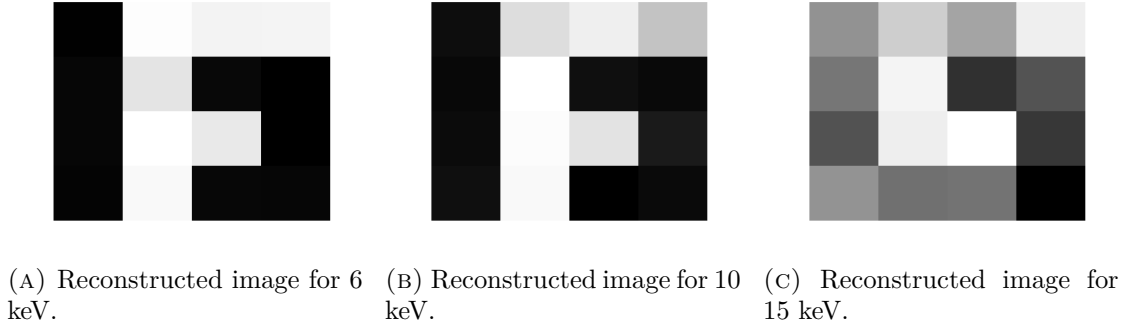
FIGURE 5.5: Results for mono-energetic sources.

beams get absorbed by the mask and the object in those cases, and in the open pixels, the photons still are detected. If the energy is too low, there is the possibility of these not getting detected, as shown in Section 4.5.1. In the case of 15 keV, without having previous knowledge of the object, it is not possible to detect the letter F. These results are clear by the *CNR* values presented in table 5.2, too.

5.1.3 Rectangular Pulses

To further explore the results obtained in the previous subsection, we simulated for ranges of 2 keV from 2 keV to 14 keV. By carrying out these simulations, a more direct comparison with the experimental results is possible.

(A) Reconstructed image for a range from 2 keV to 4 keV.

(B) Reconstructed image for a range from 4 keV to 6 keV.

(C) Reconstructed image for a range from 6 keV to 8 keV.
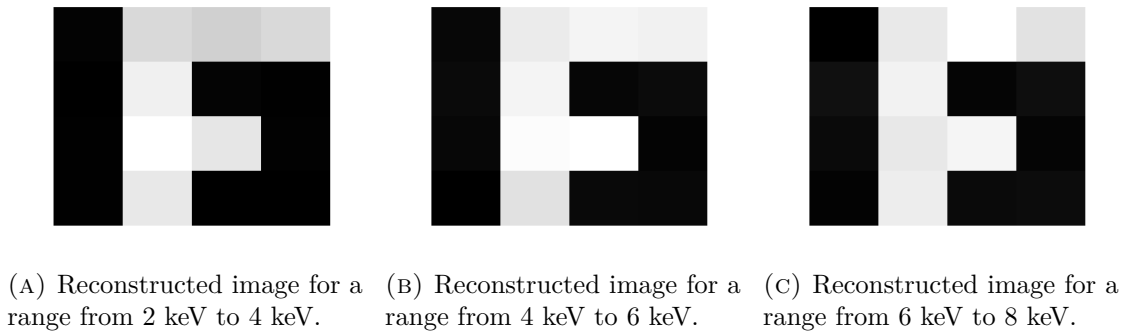
FIGURE 5.6: Results for rectangular pulses.

Only from observation of the images reconstructed (Figure 5.6 and Figure 5.7), it is possible to verify what had been proposed in the previous section. Although, when analysing the *CNR* values (table 5.3), we notice that the first interval from 2-4 keV shows a value slightly lower. If we then check the absorption spectrum of the detector (Figure 4.26), it is perceivable the concordance with the results since for 0.2 mm of
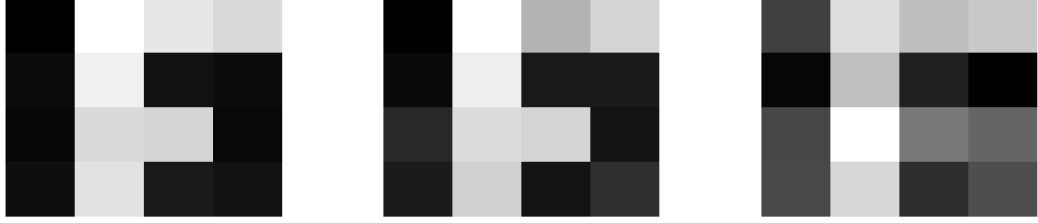
(A) Reconstructed image for a range from 8 keV to 10 keV.

(B) Reconstructed image for a range from 10 keV to 12 keV.

(C) Reconstructed image for a range from 12 keV to 14 keV.

FIGURE 5.7: Results for rectangular pulses.

TABLE 5.3: *CNR* values obtained for 2 keV -wide energy ranges.

	CNR
2-4 keV	15.0882
4-6 keV	23.4608
6-8 keV	22.2018
8-10 keV	13.9833
10-12 keV	7.4700
12-14 keV	2.9362

Polylactic Acid Filament (*PLA*), the case of the open pixels, the absorption only begins at approximately 3 keV, so the efficiency of the detector is lower. This spectrum also justifies the results for high energies, plus the fact that the high energy beams are less affected by the masks and the object.
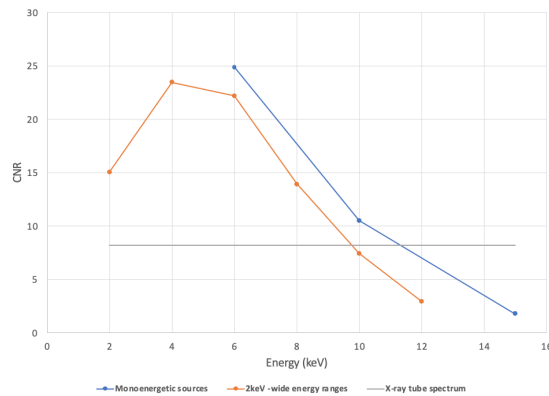
FIGURE 5.8: Plot of the *CNR* for the different energy sources using the 5 mm *PLA* masks.

The mono-energetic sources and the 2keV-wide energy ranges show a similar decreasing trend from 6 keV. For lower values, in the case of the energy ranges, the *CNR* also diminishes. The reasons for these will be explained with more detail ahead. The X-Ray tube spectrum presents a *CNR* value slightly lower than the average of the other curves.

5.1.4 Different Thicknesses

Finally, some preliminary tests were performed this time regarding the masks. The masks' thickness was altered to identify a minimum limit to form an image. It was tested for 0.2 mm, 1 mm, 2 mm, 3 mm and 4 mm. For this particular cases, the material of the object was set to iron in order to observe only the effect of the masks, since this metal is much denser, and with a reduced X-ray transmission. The energy distribution used was the X-ray tube spectrum. A simulation for 5 mm was also performed, as a comparison for the different material of the object.
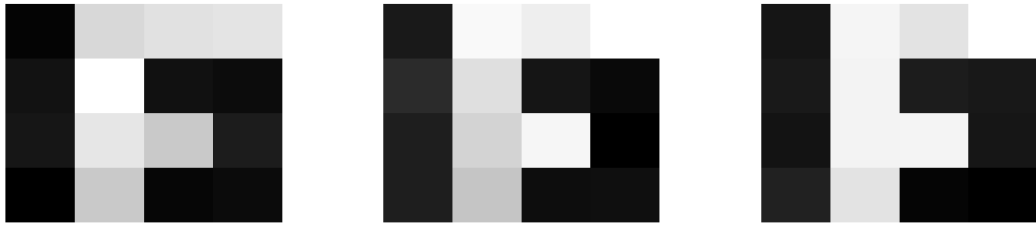
(A) Reconstructed image for 5 mm mask.

(B) Reconstructed image for 4 mm mask.

(C) Reconstructed image for 3 mm mask.

FIGURE 5.9: Results for different mask thickness with an object made of iron.
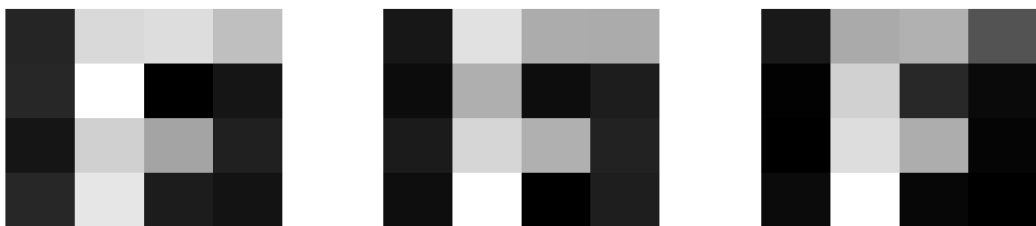
(A) Reconstructed image for 2 mm mask.

(B) Reconstructed image for 1 mm mask.

(C) Reconstructed image for 0.2 mm mask.

FIGURE 5.10: Results for different mask thickness with an object made of iron.

TABLE 5.4: *CNR* values obtained for different mask thicknesses.

	CNR
5 mm	10.6555
4 mm	8.9590
3 mm	15.9599
2 mm	6.3208
1 mm	5.4458
0.2 mm	3.3347

Figures 5.9 and 5.10 show the final images. In all cases cases, we can see that the object is detectable. For 5 mm, with the new object, the *CNR* improved, as expected, since iron is less transmittable than *PLA*. As thickness diminishes, and the transmission increases, so does the contrast in the images. The *CNR* values demonstrate this difference in sharpness.
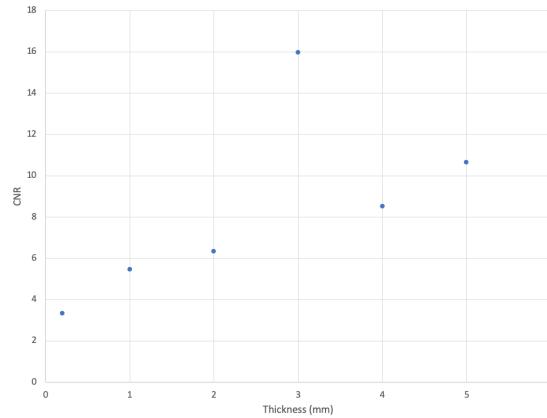
FIGURE 5.11: Plot of the *CNR* for different mask thicknesses with the X-ray Tube spectrum and an object made of iron.

Regarding the thickness evaluation, we may draw the conclusion that the *CNR* is proportional to the thickness employed, which is consistent with the fact that the X-ray transmission decreases as the thickness increases, eventually saturating for a thickness large enough. The outlier at the thickness of 3 mm was not completely understood and can be related to statistical fluctuations in the data or issues related with the simulation process.

5.2 Experimental Results

5.2.1 Experimental Setup

In Figure 5.12, it is possible to observe the distance from the X-ray tube to the detector of 2.5 m, necessary to guarantee that the X-ray photons reached the detector perpendicularly. For the alignment of the X-ray tube, a laser goniometer was used. The figure on the right demonstrates how the screws in the corners and the puzzle-like design were used to achieve the reproducible positions of the object in regard to the mask and the mask in relation to the detector.
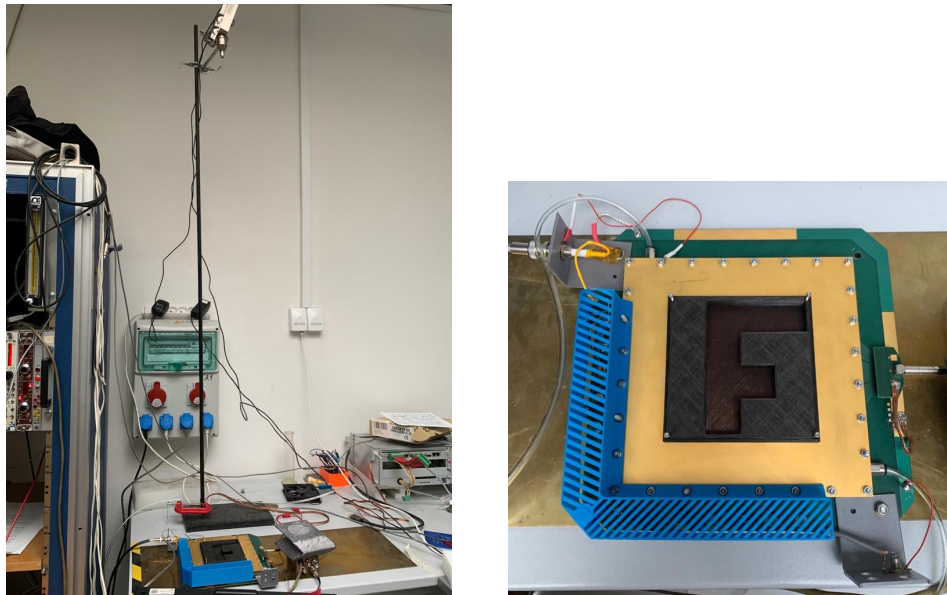
FIGURE 5.12: Left: Final experimental setup. Right: Close-up picture of the detector assembly.

5.2.2 Data Acquisition and Analysis

For the data acquisition, the X-Ray Tube was turned on and different interval times per mask were measured: 30 seconds, 1 minute, 2 minutes and 5 minutes. In all cases, a .dat file from the *Analog-to-Digital Converter* (*ADC*) was obtained for each mask, containing a spectrum, so 32 in total.

After gathering all data, the data analysis consisted of two parts:

- Data processing and determination of number of events;

- Reconstruction and calculation of the *CNR*.

The first part was implemented in *Root* software. The code started by reading the .dat files and calculating a Gaussian fit for each spectrum. Since, as mentioned in Section 4.5.4, the peak changed throughout the day, a peak position correction step was added before the determination of the number of events. In this step, a correction factor for each mask was determined by dividing each centroid by the centroid of the first mask. After multiplying all values by the corresponding correction factor, the peaks were positioned accordingly with the first one. This step was crucial to ensure that the following calculation used the same range of energies. The number of events was obtained through the integration of the peak and was performed for different ranges, in order to determine an optimal energy range. Figure 5.13 schematically presents the process described.
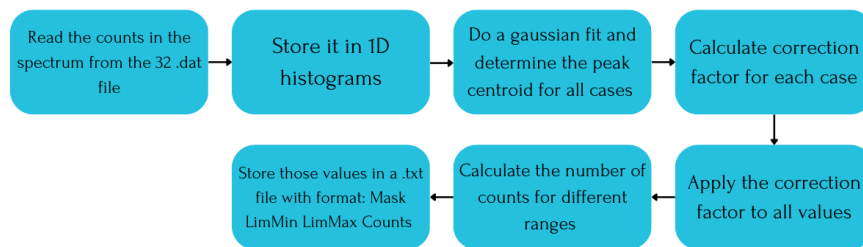
FIGURE 5.13: Scheme of the first step of data analysis: processing and determination of number of events.

In the second part, the reconstruction formula was used to calculate the final coefficients for the different energy ranges. Before actually reconstruct a final image, the *CNR* values for all cases were calculated and the best one was determined. Finally, the program returned only the image with best *CNR*, the respective contrast noise and range. Figure 5.14 represents a scheme of the program pipeline.
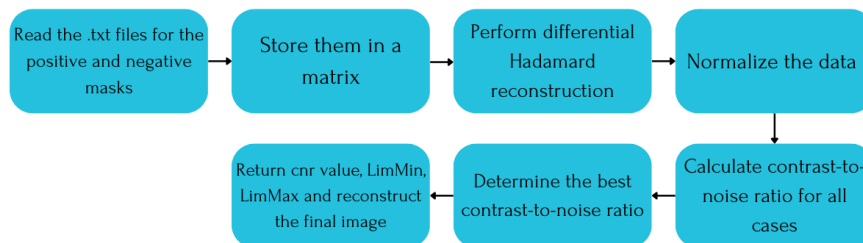
FIGURE 5.14: Scheme of the second step of data analysis: Reconstruction and calculation of the *CNR*.

5.2.3 Reconstruction

The experimental results obtained are presented in Figures 5.15 and 5.16.
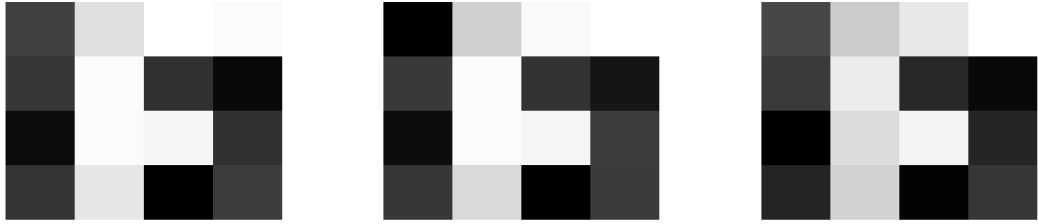
(A) Reconstructed image for 30 seconds.

(B) Reconstructed image for 1 minute.

(C) Reconstructed image for 1 minute.

FIGURE 5.15: Experimental results for different acquisition times. A) 30 seconds. B) 1 minute. C) 1 minute.
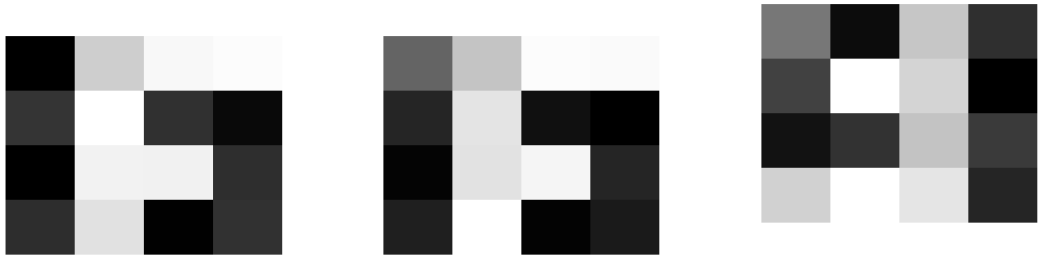
(A) Reconstructed image for 2 minutes.

(B) Reconstructed image for 5 minutes.

(C) Reconstructed image for 1 minute with the object inverted.

FIGURE 5.16: Experimental results for different acquisition times and an object inverted. A) 2 minutes. B) 5 minutes. C) 1 minute with the object inverted.

In table 5.5, the respective *CNR* values are presented and plotted in Figure 5.17.

TABLE 5.5: *CNR* values obtained for the experimental part.

	CNR
30 seconds	8.2379
1 minute, case 1	6.9231
1 minute, case 2	7.2226
2 minutes	7.6048
5 minutes	8.9222
1 minute, object inverted	5.8199
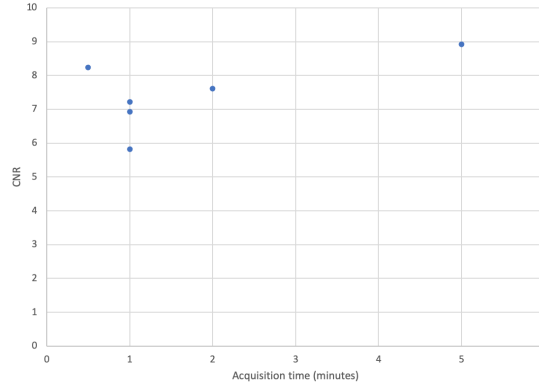
FIGURE 5.17: *CNR* as a function of the acquisition time per mask of the experimental part.

The figures obtained demonstrate the feasibility of the technique, since in all of them we can clearly identify the letter F. In all cases, in the top left corner of the original orientation images, some grey pixels that should be white are present, which would be consistent with the disparity mentioned in Section 4.5.4. Although, these are also present in the case for the inverted object, so a final conclusion cannot be made. As for the *CNR* values, all of them are close. This can lead to the conclusion that, in this case, larger intervals of time will not necessaryly further improve the results, possibly because of the detector non-uniformity through time. Furthermore, shorter time intervals can still be evaluated in order to establish a minimum limit that still provides enough statistics, since, for 30 seconds, the image has not shown any sign of worsening, having, in fact, one of the best *CNR* of 8.24.

5.3   Discussion

Comparing the simulation and experimental results, it is clear that, although the experimental measurements obtained good results, these still cannot reach the contrast and image quality obtained in the simulation. Regarding the masks (and object), the 3D printer used is not able to produce a 100% compact pieces, what would consequently alter the density of the masks, and allow for more X-ray transmission through the material, compared to the simulation. Concerning the X-ray tube, it is possible that, even with the distance used to the detector, some photons reached the detector diagonally, intercepting different positions in the object, mask and active area. In the simulation, a square flat source with the dimensions of the detector was defined, and a perpendicular travel direction was set, eliminating this risk. In addition, the features of the detector

have to be taken into account, particularly the non-uniformity in area and in time already discussed. Possibly due to the latter, in the experimental part, the *CNR* does not increase with the increase of the acquisition time. In the simulations, since no charging up occurs, with more statistics, the *CNR* has shown to improve.

Chapter 6

Conclusion

The objective of this project was to prove the feasibility of X-ray *Single-Pixel Imaging* (*SPI*). The proof of concept was successfully made, both computationally and experimentally.

Relying on simulations, the material and thickness chosen for the masks were $5\,\mathrm{mm}$ *Polylactic Acid Filament* (*PLA*) masks, with a transmission value of 0.00026%, for a 55Fe source. To complement these results, the transmission was also determined experimentally, obtaining a value of 0.67%, for the 55Fe source and compared with the simulations. Although a notorious difference can be verified, *PLA* filament proved to absorb enough radiation, presenting itself as an alternative to the metals usually used, reducing the total cost of the setup.

In addition, a functional triple *Gas Electron Multiplier* (*GEM*) detector was built and characterized in terms of energy resolution, detector gain and uniformity. The values obtained were in accordance with the literature. We obtained a gain of around 10^4 as planned and an energy resolution of around 30%. An advantage of using a *GEM* detector with *SPI* is the fact that it is immune to the noise caused by the X-ray fluorescence from the copper layers of the *GEM*s. In fact, these photons even "artificially" increase the efficiency of the detector, by increasing the number of counts.

The results for the simulations of the entire system have shown better results than for the experimental setup, as expected. In fact, to take into account effects related to the detector, such as non uniformities in its construction that lead to position dependent gain, energy resolution; electronic noise, detector charging up effects related to the intensity of the radiation field, among others; a deeper simulation study outside the scope of this work would be necessary. A relation between the *Contrast-to-Noise Ratio* (*CNR*) and the range of energies can be observed in accordance with the expected detector

response calculated. The range from 4 keV to 6 keV demonstrated the best performance with a *CNR* of 23.5. As for the experimental results, an average *CNR* of 7.46 was obtained. The acquisition time per mask and the *CNR* did not present a clear proportional relation, due to the statistical fluctuations created by the detector.

6.1 Limitations and Future Work

Although the experimental setup performed well, some aspects can still be improved. Regarding the detector, an optimization of the detector assembly can still be done, in order to possibly reduce the charging up effect [59]. That would also help in the improvement of the area non-uniformity.

Concerning the *PLA* masks, the values for the transmission achieved were far from the expected from simulations, which led to believe the 3D printer could not achieve the 100% density. The use of a state-of-the-art 3D printer could attenuate this effect, since these have more infill options and an optimized printing process compared to the one used. Since a 4×4 pixel image was successfully reconstructed, the next step could also be to increase the number of pixels on the masks, emphasizing the importance of an improved 3D printer. By increasing the number of pixels, a more complex object could also be chosen.

Since each mask had to be placed on top of the detector individually and the source had to be turned off during this process due to the risk that X-rays pose to people, an improvement that might shorten the overall acquisition time is to automate the mask-changing procedure.

In our case, as already has been said, a simple inverse transform was used for the reconstruction. If more complex objects and more pixels were used, than more elaborate algorithms might be used, such as *Total Variation Minimization by Augmented Lagrangian and Alternating Direction Algorithm* (*TVAL3*).

Other potential applications of this technique includes X-ray fluorescence imaging and X-ray imaging through a diffuse media. For the first case, a setup as represented in [60] can be assembled, placing the masks adjacent to the detector, as in the setup for this work. For the second case, a similar setup to the used in this work can be designed, adding only a diffuse media between the source and the sample.

Bibliography

[1] W. C. Röntgen. *Über eine neue art von strahle.* Translation into Portuguese: A. C. P. Carvalho, Sobre uma nova espécie de raios, Rev. Imagem, 27(4):287 – 293, 2005. Aus den Sitzungsberichten der Würzburger Physik.-medic, 1895.

[2] Xiangyu Ou et al. "Recent development in x-ray imaging technology: Future and challenges". In: *Research* 2021 (2021).

[3] Philip J Withers et al. "X-ray computed tomography". In: *Nature Reviews Methods Primers* 1.1 (2021), p. 18.

[4] G. Pang Y. Tian. "Experimental study of a single-pixel prototype anti-scatter detector for megavoltage x-ray imaging". In: *ELSEVIER* (2015). DOI: `http://dx.doi.org/10.1016/j.radphyschem.2015.09.006`.

[5] Pedro G. Vaz et al. "Re-Ordering of Hadamard Matrix Using Fourier Transform and Gray-Level Co-Occurrence Matrix for Compressive Single-Pixel Imaging in Low Resolution Images". In: *IEEE Access* 10 (2022), pp. 46975–46985. DOI: `10.1109/ACCESS.2022.3171334`.

[6] Patrıcia P Santos et al. "Compressive single pixel phosphorescence lifetime and intensity simultaneous imaging: a pilot study using oxygen sensitive biomarkers". In: *Integrated Optics: Design, Devices, Systems and Applications VI*. Vol. 11775. SPIE. 2021, pp. 142–152.

[7] Yu-Hang He et al. "High-resolution sub-sampling incoherent x- ray imaging with a single-pixel detector". In: *APL Photonics* 5.056102 (2020). DOI: `https://doi.org/10.1063/1.5140322`.

[8] Pedro G. Vaz, Beatriz Guerra, and João Cardoso. "Single-pixel imaging: concepts and application to imaging through scattering media". In: *2023 23rd International Conference on Transparent Optical Networks (ICTON)*. 2023, pp. 1–9. DOI: `10.1109/ICTON59386.2023.10207213`.

[9]   Marco F. Duarte et al. "Single-pixel imaging via compressive sampling". In: *IEEE Signal Processing Magazine* 25.2 (2008), pp. 83–91. DOI: 10.1109/MSP.2007.914730.

[10]   Glenn F. Knoll. *Radiation Detection and Measurement.* fourth. John Wiley & Sons, Inc., 2010.

[11]   Andreas Maier et al. *Medical Imaging Systems: An Introductory Guide.* SpringerOpen, 2018.

[12]   X-ray Consultant for the Electronics Industry Dr. David Bernard. *History of X-rays – 125 years in the making (pt 2).* https://www.excillum.com/history-of-x-rays-x-ray-tubes/. [Online; accessed 04-July-2023].

[13]   J. Anthony Seibert. "X-Ray Imaging Physics for Nuclear Medicine Technologists. Part 1: Basic Principles of X-Ray Production". In: *Journal of Nuclear Medicine Technology* 32.3 (2004), pp. 139–147. ISSN: 0091-4916. URL: https://tech.snmjournals.org/content/32/3/139.

[14]   A.-L Manninen. "Clinical Applications Of Radiophotluminesce (RPL) Dosimetry In Evaluation Of Patient Radiation Exposure In Radiology: Determination of absorbed and effective dose". PhD thesis. Nov. 2014.

[15]   ExpertsMind. *Pair Production Assignment Help.* https://www.expertsmind.com/topic/radiation-types/pair-production-99281.aspx. [Online; accessed 05-July-2023].

[16]   Fernando Domingues Amaro et al. "The CYGNO experiment". In: *Instruments* 6.1 (2022), p. 6.

[17]   Marcia Dutra R. Silva. "Ionizing Radiation Detectors". In: *Evolution of Ionizing Radiation Research.* Ed. by Mitsuru Nenoi. Rijeka: IntechOpen, 2015. Chap. 8. DOI: 10.5772/60914. URL: https://doi.org/10.5772/60914.

[18]   Radiopaedia. *Operating regions of gaseous ionization detectors.* https://radiopaedia.org/cases/operating-regions-of-gaseous-ionisation-detectors. [Online; accessed 06-July-2023].

[19]   Thaddeus J. Trenn. "The Geiger-Müller Counter of 1928". In: *Annals of Science* 43.2 (1986), pp. 111–135. DOI: 10.1080/00033798600200171. URL: https://doi.org/10.1080/00033798600200171.

[20]   Wikipedia. *Townsend discharge.* https://en.wikipedia.org/wiki/Townsend_discharge. [Online; accessed 10-July-2023].

[21]   Hugo Natal da Luz. "Development of neutron and X-ray imaging detectors based on MHSP". PhD thesis. Ph. D. Thesis, 2009.

[22] Fabio Sauli. *Gaseous radiation detectors: fundamentals and applications*. Cambridge University Press, 2015.

[23] Georges Charpak and Fabio Sauli. "Multiwire proportional chambers and drift chambers". In: *Nuclear Instruments and Methods* 162.1-3 (1979), pp. 405–428.

[24] Fabio Sauli. "Principles of operation of multiwire proportional and drift chambers". In: *Geneva, Switzerland* (1977).

[25] Maxim Titov. *Gaseous Detectors: recent developments and applications*. 2010. arXiv: 1008.3736 [physics.ins-det].

[26] Fabio Sauli and Archana Sharma. "MICROPATTERN GASEOUS DETECTORS". In: *Annual Review of Nuclear and Particle Science* 49.1 (1999), pp. 341–388. DOI: 10.1146/annurev.nucl.49.1.341. eprint: https://doi.org/10.1146/annurev.nucl.49.1.341. URL: https://doi.org/10.1146/annurev.nucl.49.1.341.

[27] Fabio Sauli. "The gas electron multiplier (GEM): Operating principles and applications". In: *Nuclear Instruments and Methods in Physics Research Section A: Accelerators, Spectrometers, Detectors and Associated Equipment* 805 (2016). Special Issue in memory of Glenn F. Knoll, pp. 2–24. ISSN: 0168-9002. DOI: https://doi.org/10.1016/j.nima.2015.07.060. URL: https://www.sciencedirect.com/science/article/pii/S0168900215008980.

[28] W. Bonivento et al. "A complete simulation of a triple-GEM detector". In: *IEEE Transactions on Nuclear Science* 49.4 (2002), pp. 1638–1643. DOI: 10.1109/TNS.2002.805170.

[29] Rajendra Nath Patra et al. "Measurement of basic characteristics and gain uniformity of a triple GEM detector". In: *Nuclear Instruments and Methods in Physics Research Section A: Accelerators, Spectrometers, Detectors and Associated Equipment* 862 (2017), pp. 25–30. ISSN: 0168-9002. DOI: https://doi.org/10.1016/j.nima.2017.05.011. URL: https://www.sciencedirect.com/science/article/pii/S0168900217305405.

[30] Pedro G. Vaz et al. "Image quality of compressive single-pixel imaging using different Hadamard orderings". In: *Opt. Express* 28.8 (Apr. 2020), pp. 11666–11681. DOI: 10.1364/OE.387612. URL: https://opg.optica.org/oe/abstract.cfm?URI=oe-28-8-11666.

[31] Emmanuel J Candès and Michael B Wakin. "An introduction to compressive sampling". In: *IEEE signal processing magazine* 25.2 (2008), pp. 21–30.

[32] Zibang Zhang et al. "Hadamard single-pixel imaging versus Fourier single-pixel imaging". In: *Optics Express* (Aug. 2017). DOI: `https://doi.org/10.1364/OE.25.019619`.

[33] Lourdes López-Garcıa et al. "Efficient ordering of the Hadamard basis for single pixel imaging". In: *Optics Express* 30.8 (2022), pp. 13714–13732.

[34] Wolfram MathWorld. *Kronecker Product.* https://mathworld.wolfram.com/KroneckerProduct.html. [Online; accessed June-2023].

[35] Graham M. Gibson, Steven D. Johnson, and Miles J. Padgett. "Single-pixel imaging 12 years on: a review". In: *Optics Express* 28.28190 (Sept. 2020).

[36] Margie P. Olbinado et al. "X-ray phase-contrast ghost imaging using a single-pixel camera". In: *Optica* 8.437481 (2021). DOI: `https://doi.org/10.1364/OPTICA.437481`.

[37] AI-XIN ZHANG et al. "Tabletop x-ray ghost imaging with ultra-low radiation". In: *Optica* 5.306676 (2018). DOI: `https://doi.org/10.1364/OPTICA.5.000374`.

[38] Daniele Pelliccia et al. "Experimental X-Ray Ghost Imaging". In: *PHYSICAL REVIEW LETTERS* 117.113902 (Sept. 2016). DOI: `10.1103/PhysRevLett.117.113902`.

[39] A. Schori and S. Shwartz. "X-ray ghost imaging with a laboratory source". In: *Optics Express* 25 (June 2017). DOI: `http://doi.org/10.1364/OE.25.014822`.

[40] Y. Klein et al. "X-ray computational ghost imaging with single-pixel detector". In: *Opt. Express* 27.3 (Feb. 2019), pp. 3284–3293. DOI: `10.1364/OE.27.003284`. URL: `https://opg.optica.org/oe/abstract.cfm?URI=oe-27-3-3284`.

[41] Hong Yu et al. "Fourier-Transform Ghost Imaging with Hard X Rays". In: *Phys. Rev. Lett.* 117 (11 Sept. 2016), p. 113901. DOI: `10.1103/PhysRevLett.117.113901`. URL: `https://link.aps.org/doi/10.1103/PhysRevLett.117.113901`.

[42] Yu-Hang He et al. "Single-pixel imaging with neutrons". In: *Elsevier* (Sept. 2020). DOI: `https://doi.org/10.1016/j.scib.2020.09.030`.

[43] Zhuoyao Huang et al. "Multimodality system of x-ray and fluorescence based on Fourier single-pixel imaging for small animals". In: *Journal of Biomedical Optics* 27.9 (2022), p. 090501. DOI: `10.1117/1.JBO.27.9.090501`. URL: `https://doi.org/10.1117/1.JBO.27.9.090501`.

[44] Minghui Zhang et al. "Lensless Fourier-transform ghost imaging with classical incoherent light". In: *Phys. Rev. A* 75 (2 Feb. 2007), p. 021803. DOI: `10.1103/PhysRevA.75.021803`. URL: `https://link.aps.org/doi/10.1103/PhysRevA.75.021803`.

[45] Tomoyoshi Shimobaba et al. "Computational ghost imaging using deep learning". In: *Optics Communications* 413 (2018), pp. 147–151. ISSN: 0030-4018. DOI: `https://doi.org/10.1016/j.optcom.2017.12.041`. URL: `https://www.sciencedirect.com/science/article/pii/S0030401817311628`.

[46] Andrew Maurice Kingston et al. "X-Ray Ghost-Tomography: Artefacts, Dose Distribution, and Mask Considerations". In: *IEEE Transactions on Computational Imaging* 5.1 (2019), pp. 136–149. DOI: `10.1109/TCI.2018.2880337`.

[47] Andrew J. Gilbert et al. "A single-pixel X-ray imager concept and its application to secure radiographic inspections". In: *ELSEVIER* (2017). DOI: `http://dx.doi.org/10.1016/j.nima.2017.03.028`.

[48] AMPTEK. *Mini-X X-Ray Tube.* https://www.amptek.com/internal-products/obsolete-products/mini-x-x-ray-tube-software. [Online; accessed December-2022].

[49] C Altunbas et al. "Construction, test and commissioning of the triple-GEM tracking detector for COMPASS". In: *Nuclear Instruments and Methods in Physics Research Section A: Accelerators, Spectrometers, Detectors and Associated Equipment* 490.1-2 (2002), pp. 177–203.

[50] CAEN. *Power Supply Module N8034.* https://www.caen.it/products/n8034/. [Online; accessed March-2023].

[51] Physics Open Lab. *PMT Pulse Processing.* https://physicsopenlab.org/2016/04/21/pmt-pulse-processing/. [Online; accessed July-2023]. 2016.

[52] Rita Joana da Cruz Roque. "X-ray imaging using 100 um thick Gas Electron Multipliers operating in Kr-CO2 mixtures". MA thesis. Universidade de Coimbra, 2018.

[53] ORTEC. *142A/B/C Preamplifiers.* https://www.ortec-online.com/products/electronics/preamplifiers/142a-b-c. [Online; accessed February-2023].

[54] Canberra. *Model 2111 Timing Filter Amplifier.* http://phy.fiu.edu/pub/TWiki/MAST_Diagnostic/Equipment_Amplifier.pdf. [Online; accessed July-2023].

[55] Canberra. *Canberra ADC 8713 module.* http://www.nuclearphysicslab.com/npl/wp-content/uploads/canberra_8713_Analog_Digital_Converter.pdf. [Online; accessed July-2023].

[56]   Vogtlin instruments. *High-precision Thermal Mass Flow Meters & Mass Flow Controllers for Gases.* https://www.voegtlin.com/en/mass-flow-meters-and-controllers-for-gases/red-y-smart-series/?gclid=Cj0KCQjwuNemBhCBARIsADp74QSQ3PvB 8lSQmF5P424cE6usYHNy6OtiB0AiDJCQ0yf1TxzgbOZVDAEaAhLdEALw_wcB. [Online; accessed August-2023].

[57]   Prusa. *Infill patterns.* https:// help.prusa3d.com/article/infill-patterns__177130. [Online; accessed March-2023].

[58]   Center for X-Ray Optics at Lawrence Berkeley National Laboratory. *X-Ray Interactions With Matter.* `https://henke.lbl.gov/optical_constants/`. [Online; accessed March-2023].

[59]   M Alfonsi et al. "Simulation of the dielectric charging-up effect in a GEM detector". In: *Nuclear Instruments and Methods in Physics Research Section A: Accelerators, Spectrometers, Detectors and Associated Equipment* 671 (2012), pp. 6–9.

[60]   Geovane GA de Souza and Hugo Natal da Luz. "XRF element localization with a triple GEM detector using resistive charge division". In: *Nuclear Instruments and Methods in Physics Research Section A: Accelerators, Spectrometers, Detectors and Associated Equipment* 937 (2019), pp. 141–147.